Wind Load Analysis on

a High-rise Square-plan Building

by

Xitong Zhu

A Thesis Presented in Partial Fulfillment
of the Requirements for the Degree
Master of Science

Approved July 2014 by the
Graduate Supervisory Committee:

Keith Hjelmstad, Chair
Subramaniam Rajan
Apostolos Fafitis

ARIZONA STATE UNIVERSITY

August 2014

ABSTRACT

Buildings and other structures, all components and cladding thereof, shall be designed and constructed to resist the wind loads are required in all wind codes. Simple quasi-static treatment of wind loads, which is universally applied to design of low to medium-rise structures, can be either overly conservative or erroneous under-estimated for design of high-rise structures. Dynamic response, vortex, wind directionality, and shedding from other structures are all complicated key factors suppose to be considered in design. Meanwhile, wind tunnel testing is expansive, difficult and sometimes inaccurate even if it is a widely used method in simulation of aerodynamic response. Computational Fluid dynamics (CFD), historically, were two-dimensional (2D) method using conformal transformations of the flow about a cylinder to the flow about an airfoil were developed in the 1930s. A number of three-dimensional (3D) codes were developed, leading to numerous commercial packages, which is more accessible and economical for wind load analysis.

ACKNOWLEDEMENTS

First of all, I wish to extend an especial acknowledgement to my graduate advisor Dr. Keith Hjelmstad, who not only helped me tremendously in my academic endeavors during the two years of graduate study, but also enlightened me as an engineer. I would also like to acknowledge Dr. Apostolos Fafitis and Dr. Subramaniam Rajan for their knowledge and advices, which contribute significantly in my entire procedure of study.

Finally, I want to thank my parents for their support in my life.

TABLE OF CONTENTS

Page

CHAPTER Page

LIST OF TABLES

Table Page

LIST OF FIGURES

Figure Page

Figure Page

Figure Page

Figure Page

1 INTRODUCTION

The majorities of practical fluid flows are turbulent with many complex flow features, which may contain recirculation zones and flow stagnation points. The types of flows encountered in the field of wind engineering are no exception.

Due to the complexity of wind flow, all the research and design work undertaken in this field has concentrated on the use of full-scale and wind tunnel analysis. This has involved the use of expensive wind tunnel and data recording facilities and has required significant time and effort to obtain the desired results. However during the 1970's and 1980's there was a great deal of interest among the engineering community into a relatively new technique known as computational fluid dynamics (CFD). The advances made in high-speed digital computer technology had enabled the solution of flow problems, which were described mathematically by a set of coupled nonlinear partial differential equations and the appropriate boundary conditions, in a relatively short space of time and for a low financial cost. Initially the wind engineering community largely ignored this technique due to the need for powerful computers and the errors in early modeling techniques. Nonetheless, the rapidly falling costs of computer hardware and further advances in technology in the late 1980's and early 1990's enabled CFD to be applied to the complex field of wind engineering.

Figure 1.1.1 Vortex Shedding on John Hancock Center

In theory it is numerically possible to completely resolve all aspects of a fluid dynamics problem including the rapid spatial and temporal variations of turbulence in the flow using a CFD technique known as direct numerical simulation. This technique involves discretizing the equations using the finite volume method at a mesh size below the smallest eddies in turbulent flow, the Kolmorogov length scale, and therefore resolving the flow down to the smallest spatial and temporal variations. Unfortunately the direct numerical simulation of practical turbulent fluid flows using the time dependent Navier-Stokes equations in their simplest form is well beyond the capabilities of present day computing power. This is due to the fact that the amount of computer processing (CPU) time required is dependent on the degree of resolution of the small scale eddies. The smallest eddies in turbulent flow, the so-called 'Kolmogorov microscale', are at about 0.1 to 1mm for natural air. Therefore the numerical discretization of entire wind

engineering flow field with a complex geometry at high Reynolds numbers is at present well beyond the capabilities of even the most powerful supercomputer on earth.

An economically feasible way to solve this problem is to employ statistically averaged equations, which govern the mean flow equations. Turbulence models are then required to achieve closure of the averaged equations and represent the action of turbulent stresses on the mean flow. Unfortunately the mathematical models used in CFD are only able to perform the physical assumptions and knowledge built into them. In particular the assumptions made regarding the modeling of the turbulent component of engineering flows have proved to be a major source of error in wind engineering simulations.

Presently, the most popular and widely used models use equations to represent a single length and velocity scale and are based on Reynolds averaging and the isotropic eddy viscosity concept. Although many of these turbulence models have been used successfully in aeronautical applications, in which fluid flow without separation may be a regular occurrence the same is not true of wind engineering applications. Wind engineering flow fields are highly complex and are characterized by the presence of multiple recirculation zones embedded within a unidirectional flow. The addition of streamline curvature and favorable and adverse pressure gradients leads to flow fields possessing very different turbulence scales and structures. Consequently such turbulence models have great difficulty in simulating wind engineering flow fields, which are essentially transient and highly anisotropic.

It is therefore apparent that one of the main obstacles to the use of CFD in wind engineering is that of turbulence modeling.

This work has concentrated on a turbulence model and analyzed its effects on the accuracy of the results obtained for bluff body flow simulations in the Abaqus CFD. A number of bluff body test cases have been used, which are compared with ASCE 7-10 wind code, rather than experiment data.

2 BOUNDARY-LAYER AND SURFACE PROCESSES

2.1 Introduction

The boundary layer is the region of the atmosphere between the Earth's surface and 500–3000 m height that is influenced substantially by energy and moisture from the surface. The bottom ten percent of the boundary layer is the surface layer. Some parameters that affect the surface layer and boundary layer are ground temperature, soil moisture, and turbulent fluxes. In this chapter, equations of eddy diffusion coefficients for momentum and energy are derived. Analytical equations for the vertical profile of wind speed are provided.

2.2 Turbulent Fluxes of Momentum

Turbulence is due to wind shear and buoyancy (thermal turbulence). Turbulence mixes gradients of momentum, energy, moisture, gases, and particles vertically and horizontally. In a model, the degree of vertical mixing due to turbulence can be quantified with a turbulent flux term. In the case of vertical mixing of horizontal momentum, the term is a function of the kinematic vertical turbulent momentum flux, $w'u'$ and $w'v'$ ($m^2 \bullet s^{-1}$).

Kinematic turbulent fluxes of momentum are negatively proportional to Reynolds stresses. A Reynolds stress, which arises when a fluid undergoes turbulent motion, causes a parcel of air to deform. Suppose an air parcel fluctuates randomly in time due to mechanical shear and buoyancy. Precise scalar velocities, w and u, in the parcel have mean components $\overline{w}$ and $\overline{u}$, eddy components w' and u', respectively. A $\overline{w'}$ velocity

has the effect of mixing $\overline{u'}$ velocities in the z-direction. The vertical mixing of the $\overline{u'}$ velocity exerts a force in the x-direction over an area normal to the z-direction. The effect of the force per unit area, or stress, is to induce a drag on u¯ and to cause the air parcel to deform, as shown in Figure 2.1.1.

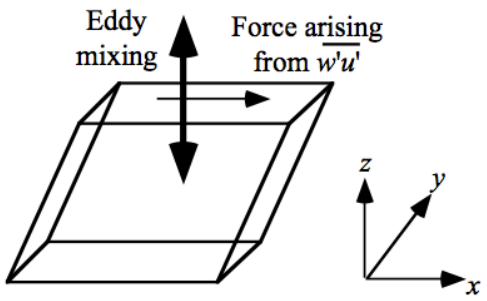

Figure 2.1.1 Deformation of a Cubic Air Parcel Caused by a Kinematic Vertical Momentum Flux w′ u′, as Described in the Text. Adapted from Stull (1988).

In the example above, the scalar component of Reynolds stress in the x-direction along a plane normal to the z-direction is

$$\tau_{zx} = -\rho_a \overline{w'u'} \tag{2.1.1}$$

(kg•m^{-1}•s^{-2} or N•m−2), where ρ_a is air density (kg•m^{-3}). This stress results from the vertical transport of a west–east gradient of momentum. Since w′ mixes u′ in the same way that u′ mixes w′, one could have u′w′ = w′u′, $\tau_{zx} = \tau_{xz}$, and $\tau_{xz} = -\rho_a u'w'$. The Reynolds stress in the y-direction along a plane normal to the z-direction is $\tau_{zy} = -\rho aw'v'$. Both τ_{zx} and τ_{zy} have the effect of transporting gradients of horizontal momentum vertically. Combining the two gives the magnitude of the vertical turbulent flux of horizontal momentum as

$$\left|\tau_z\right| = \rho_a \left[\left(\overline{w'u'} \right)^2 + \left(\overline{w'v'} \right)^2 \right]^{1/2} \tag{2.1.2}$$

(kg•m^{-1}•s^{-2}). From (2.1.1), the kinematic vertical turbulent fluxes of west–east and south–north momentum are

$$\overline{w'u'} = -\frac{\tau_{zx}}{\rho_a} \qquad \overline{w'v'} = -\frac{\tau_{zy}}{\rho_a} \tag{2.1.3}$$

When horizontal winds flow over roughness elements protruding from a surface, drag slows the wind near the surface relative to the wind aloft, creating vertical wind shear. Wind shear produces eddies that exchange momentum, energy, gases, and aerosol particles vertically. The greater the height that roughness elements protrude from a surface and the greater the horizontal wind speed, the greater the resulting wind shear and vertical flux of horizontal momentum. A scaling parameter that provides a measure of the vertical flux of horizontal momentum in the surface layer is the friction wind speed

$$u_* = \left[\left(\overline{w'u'} \right)_s^2 + \left(\overline{w'v'} \right)_s^2 \right]^{1/4} = \left(\frac{\left|\tau_z\right|}{\rho_a} \right)_s^{1/2} \tag{2.2.4}$$

The greater the friction wind speed, the greater mechanical turbulence, and the faster that momentum, energy, and pollutants from aloft mix down to the surface and vice versa. Typical roughness elements at the surface include rocks, trees, buildings, grass, and sand. The friction wind speed can be parameterized or found from field experiments in which u′, v′, and w′ are measured.

2.3 Surface Roughness Lengths

Three variables used frequently in boundary-layer parameterizations are the surface roughness lengths for momentum, energy, and moisture. The surface roughness length for momentum ($z_{0,m}$), or aerodynamic roughness, is the height above a surface at which the logarithmic profile of wind speed versus altitude extrapolates to zero wind speed. It gives a measure of vertical turbulence that occurs when a horizontal wind flows over a rough surface. The greater $z_{0,m}$, the greater the magnitude of turbulence that arises when wind passes over a roughness element. For a perfectly smooth surface, the roughness length is zero, and mechanical turbulence is minimized. For other surfaces, it is sometimes approximated as 1/30th the height of the average roughness element protruding from the surface. For surfaces with sparsely placed roughness elements, $z_{0,m}$ is the height above the base of the roughness elements (Brutsaert 1991). For densely placed roughness elements of average height h_c, $z_{0,m}$ is the height above a displacement height (d_c). Displacement heights usually lie between 0 and h_c.

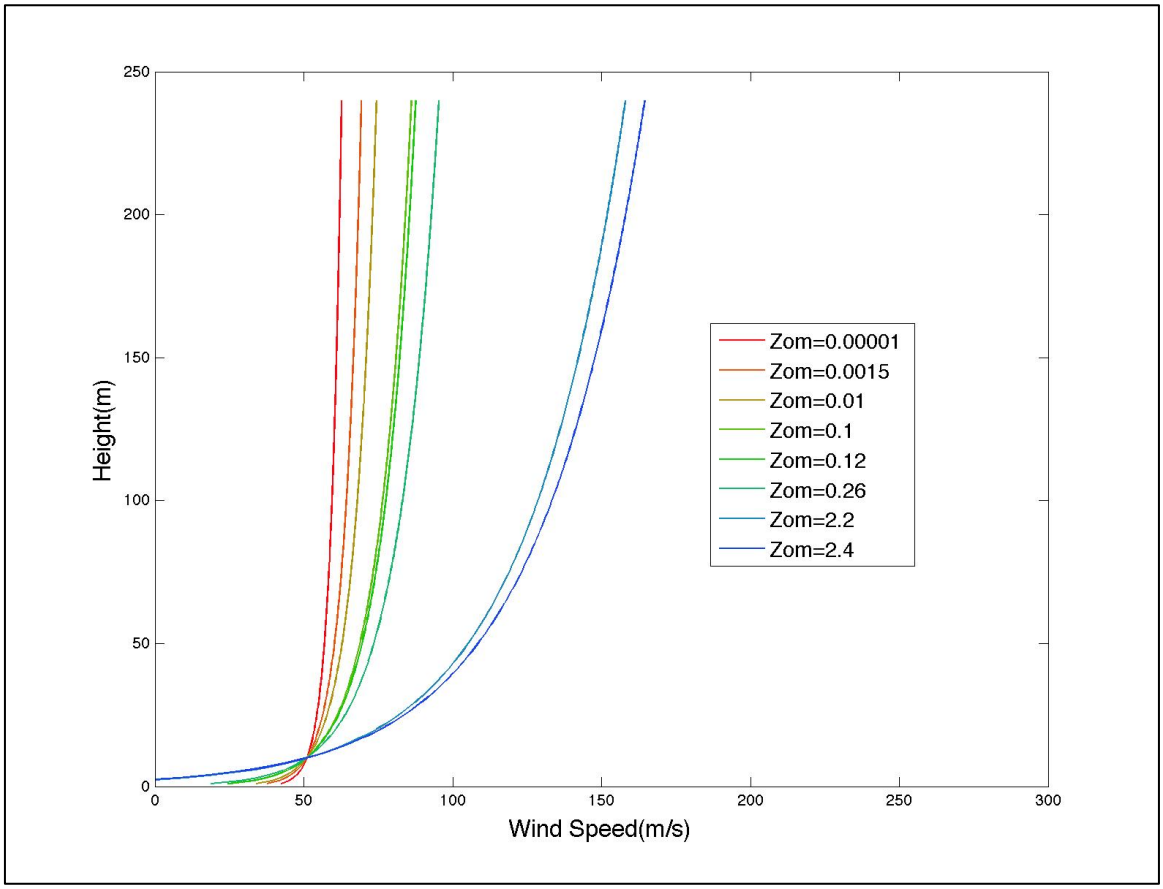

Figure 2.3.1 Data Plotted as the Height Versus Wind Speed for the Same Basic Wind Speed

Figure 2.3.1 describes a method of estimating $z_{0,m}$ from observed wind speed profiles. Parameterizations of $z_{0,m}$ from field data have also been developed. For smooth surfaces, such as over a smooth ocean with low wind speeds, one parameterization is

$$z_{0,m} \approx 0.11\frac{\upsilon_a}{u_*} = 0.11\frac{\eta_a}{\rho_a u_*} \tag{2.3.1}$$

(e.g., Hinze 1975; Garratt 1992), where $z_{0,m}$ is in m, $\nu_a = \eta_a/\rho_a$ is the kinematic viscosity of air ($m^2 \bullet s^{-1}$), η_a is the dynamic viscosity of air ($kg \bullet m^{-1} s^{-2}$) in this article picked as $1.79 \times 10^{-5} kg \cdot m^{-1} \cdot s^{-2}$, and ρ_a is air density, 1.2($kg \bullet m^{-3}$) is used in following sessions. Table 2.3.1 gives $z_{0,m}$ for several surfaces, including those with vegetation.

Table 2.3.1 Aerodynamic Roughness ($z_{0,m}$), Structure or Canopy Heights (h_c), Displacement, Heights (d_c), and Maximum One-sided Leaf Area Indices ($L_{T,max}$) for Several Surfaces (Mark z. Jacobson,2005)

Surface type	$z_{0,m}$(m)	h_c(m)	d_c(m)	$L_{T,max}$(m2 m−2)
Smooth sea	0.00001			
Rough sea	0.000015–0.0015			
Ice	0.00001			
Snow	0.00005–0.0001			
Level desert	0.0003			
Short grass	0.003–0.01	0.02–0.1	<0.075	
Long grass	0.04–0.1	0.25–1.0	0.19–0.75	
Savannah	0.4	8	4.8	
Agricultural crops	0.04–0.2	0.4–2	0.27–1.3	
Orchard	0.5–1.0	5–10	3.3–6.7	
Coniferous forest	0.28–3.9	10.4–27.5	6.3–25.3	
Tropical forest	2.2	35	29.8	
Broadleaf evergreen forest	4.8	35	26.3	7
Broadleaf deciduous trees	2.7	20	15	7
Broad- and needleleaf trees	2.8	20	15	7.5
Needleleaf evergreen trees	2.4	17	12.8	8
Needleleaf deciduous trees	2.4	17	12.8	8
Short vegetation/C4 grassland	0.12	1	0.75	5
Broadleaf shrubs w/bare soil	0.06	0.5	0.38	5
Dwarf trees and shrubs	0.07	0.6	0.45	5
Agriculture/C3 grassland	0.12	1	0.75	5
2500-m2 lot with a building 8 m high and 160-m2 silhouette	0.26	8		
25 000-m2 lot with a building 80 m high and 3200-m2 silhouette	5.1	80		

2.4 Momentum Fluxes from Similarity Theory

2.4.1 Momentum Fluxes

In the absence of wind shear above the thin surface layer, the vertical turbulent transfer of horizontal momentum is affected primarily by skin drag, form drag, and wave drag. Skin drag is the near-surface drag that results from molecular diffusion of momentum across the surface–air interface. Form drag is the near-surface drag resulting from turbulence and vertical momentum transfer that occurs when winds hit large obstacles, such as rocks or trees. Wave drag is the near-surface drag that results from vertical transfer of momentum by gravity waves, which propagate vertically and horizontally. These three types of drag are embodied in the dimensionless coefficient of drag C_D, which is used in expressions for bulk aerodynamic kinematic turbulent momentum fluxes in the surface layer,

$$\left(\overline{w'u'}\right)_s = -C_D\left|\overline{v_h}\left(z_r\right)\right|\left[\bar{u}\left(z_r\right)-\bar{u}\left(z_{o,m}\right)\right] \tag{2.4.1}$$

$$\left(\overline{w'v'}\right)_s = -C_D\left|\overline{v_h}\left(z_r\right)\right|\left[\bar{v}\left(z_r\right)-\bar{v}\left(z_{o,m}\right)\right] \tag{2.4.2}$$

Kinematic vertical turbulent fluxes of momentum and eddy diffusion coefficients for momentum can be derived from similarity theory. Substituting (2.4.1) and (2.4.2) into (2.2.3) gives the relationship between friction wind speed and the coefficient of drag as

$$u_* = \left|\bar{v}_h\left(z_r\right)\right|\sqrt{C_d} \tag{2.4.3}$$

2.4.2 MONIN–OBUKHOV SIMILARITY THEORY

In the presence of strong wind shear above the surface, bulk aerodynamic formulae are not useful. A better method of parameterizing kinematic fluxes near the surface is with Monin–Obukhov similarity theory. Similarity theory is a method by which variables are first combined into dimensionless groups. Experiments are then conducted to obtain values for each variable in the dimensionless group. The dimensionless group is then fitted, as a function of some parameter, with an empirical equation. The experiment is repeated. Usually, equations obtained from later experiments are similar to those from the first experiment. Hence, this method of obtaining an empirical equation for the dimensionless group is called similarity theory, and the relationship between the empirical equation and the dimensionless group is a similarity relationship. When similarity theory is applied to the surface layer, it is usually called Monin–Obukhov similarity theory or surface-layer similarity theory (Monin and Obukhov 1954; Stull 1988).

In this subsection, kinematic vertical turbulent fluxes and eddy diffusion coefficients are derived from similarity theory. The derivation requires the discussion of two similarity relationships and some parameters, discussed first. One similarity relationship is that for the dimensionless wind shear,

$$\frac{\phi_m}{k} = \frac{z\partial\left|\bar{v}_h\right|}{u_*\partial z} \tag{2.4.4}$$

The right side of this equation, as a whole, is dimensionless. Individual factors, such as the wind shear ($\partial|\bar{v}_h|/\partial z$) and u_*, are found from field experiments. Wind shear is measured directly, and u_* is found from (2.2.4), the terms of which are measured. The parameter φ_m/k is determined as a function of z/L by substituting measurements of $\partial|\bar{v}_h|/\partial z$ and u_* into (2.4.4) for different values of z/L and fitting curves to the resulting data. L is the Monin–Obukhov length (m), discussed shortly, and z/L is a dimensionless group. The von Ka´rma´n constant k is found by substituting measurements of $\partial|\bar{v}_h|/\partial z$ and u_* into (2.4.4) under neutral conditions, when $\varphi_m = 1$, then solving for k. Businger et al. (1971) derived φ_m from field data when k = 0.35 as

$$\phi_m = 1 + \beta_m \frac{z}{L} \qquad \frac{z}{L} > 0 \qquad \textit{stable}$$

$$\phi_m = \left(1 - \gamma_m \frac{z}{L}\right)^{-1/4} \qquad \frac{z}{L} < 0 \qquad \textit{unstable}$$

$$\phi_m = 1 \qquad \frac{z}{L} = 0 \qquad \textit{neutral} \tag{2.4.5}$$

where β_m =4.7 and γ_m =15.0.When k=0.4, the values β_m =6.0 and γ_m = 19.3 should be used instead to obtain the same values of φ_m as when k = 0.35 (Hogstrom 1988).

2.4.3 Monin–Obukhov Length

The Monin–Obukhov length (L) is a length scale (m) proportional to the height above the surface at which buoyant production of turbulence first dominates mechanical (shear) production of turbulence.

Mathematically,

$$L = -\frac{u_*^3 \bar{\theta}_v}{kg\left(\overline{w'\theta_v'}\right)_s} = \frac{u_*^2 \bar{\theta}_v}{kg\theta_*} \tag{2.4.6}$$

where θ_* is a potential temperature scale (K), discussed shortly, and the second expression is derived by substituting the similarity-theory approximation

$$\left(\overline{w'\theta'_v}\right)_s \approx -u_*\theta_* \tag{2.4.7}$$

The parameter θ_* is proportional to $\bar{\theta}_V(z_r) - \bar{\theta}_V(z_{0,h})$, the vertical difference in potential virtual temperature. The greater $\bar{\theta}_V$ at $z_{0,h}$ in comparison with its value at z_r, the more negative the change in $\bar{\theta}_V$ with increasing height, and the greater the instability of the surface layer. In such cases, L is negative but has a small magnitude, since it is inversely proportional to θ_*. When L is negative with a small magnitude, z/L is negative with a large magnitude. Such values of z/L correspond to large instability due to buoyancy. Positive values of z/L correspond to increasing $\bar{\theta}_V$ with altitude and stable stratification.

2.4.4 Dimensionless Potential Temperature Gradient

An expression for the potential temperature scale, θ_*, can be obtained from a similarity relationship for the dimensionless potential temperature gradient,

$$\frac{\phi_h}{k} \approx \frac{z}{\theta_*}\frac{\partial \bar{\theta}_v}{\partial z} \tag{2.4.8}$$

where $\partial\bar{\theta}_V/\partial z$ is the change in mean potential virtual temperature with height. Businger et al. (1971) performed experiments to find φ_h for different stability regimes when $\bar{\theta}_p$ was used instead of $\bar{\theta}_V$ and k = 0.35. The resulting parameterization was

$$\phi_m = \mathrm{Pr}_t \qquad \frac{z}{L} = 0 \qquad \textit{neutral} \tag{2.4.9}$$

where $\beta_h = 4.7$, $\gamma_h = 9.0$, and

$$\mathrm{Pr}_t = \frac{K_{m,zx}}{K_{h,zz}} \tag{2.4.10}$$

is the turbulent Prandtl number, which approximates the ratio of the eddy diffusion coefficient for momentum to that for energy. For k = 0.35, Businger et al. estimated $\mathrm{Pr}_t \approx 0.74$. Hogstrom (1988) noted that, when k = 0.4, Businger et al.'s constants should be modified to $\beta_h = 7.8$, $\gamma_h = 11.6$, and $\mathrm{Pr}_t \approx 0.95$ to obtain the same relationship as when k = 0.35. Integrating both sides of (2.4.8) between $z_{0,h}$ and z_r and solving for θ_* give

$$\theta_* = \frac{k\left[\bar{\theta}_v(z_r) - \bar{\theta}_v\left(z_{o,h}\right)\right]}{\int_{Z_{o,h}}^{Z_r} \phi_h \frac{dz}{z}} \tag{2.4.11}$$

$$\int_{zoh}^{zr} \phi_h \frac{dz}{z} = \mathrm{Prln}\frac{z_r}{z_{o,h}} \qquad \frac{z}{L} = 0 \qquad \textit{neutral} \tag{2.4.12}$$

Integrating the first equation between $z_{0,m}$ and z and the second equation between $z_{0,h}$ and z gives wind speed versus altitude as

$$\left|\bar{v}_h(z)\right| = \frac{u_*}{k}\left[\ln\left(\frac{z}{z_{o,m}}\right) - \psi_m\right] \tag{2.4.13}$$

$$\bar{\theta}(z) = \bar{\theta}_v\left(z_{o,h}\right) + \mathrm{Pr}_t\frac{\theta_*}{k}\left[\ln\left(\frac{z}{z_{o,b}}\right) - \psi_h\right] \tag{2.4.14}$$

$$\Psi_m = \int_{Z_{o,m}}^{Z} \left(1 - \phi_m\right)\frac{dz}{z} \tag{2.4.15}$$

Integrating (2.4.15) with values of φ_m

$$\psi_m = -\frac{\beta_m}{L}(z_r - z_{o,m}) \qquad \frac{z}{L} > 0 \qquad \textit{stable}$$

$$\psi_m = l\,\mathrm{n}\frac{\left(1+\phi_m(z)^{-2}\right)\left(1+\phi_m(z)^{-1}\right)^2}{\left(1+\phi_m(z_{o,m})^{-2}\right)\left(1+\phi_m(z_{o,m})^{-1}\right)^2}$$

$$-2\tan^{-1}[\phi_m(z)]^{-1} + 2\tan^{-1}[\phi_m(z_{o,m})]^{-1} \qquad \frac{z}{L} < 0 \qquad \textit{unstable}$$

$$\psi_m = 0 \qquad \frac{z}{L} = 0 \qquad \textit{neutral} \qquad (2.4.16)$$

The influence function for momentum accounts for the difference between a logarithmic wind speed profile and an actual profile under stable and unstable conditions. The influence function for energy is analogous to that for momentum.

Under neutral conditions, $\varphi_m = 0$, and (2.4.13) reduces to a standard logarithmic wind profile for a neutrally stratified surface layer,

$$\left|\bar{v}_h(z)\right| = \frac{u_*}{k}\left[\ln\left(\frac{z}{z_{o,m}}\right)\right] \qquad (2.4.17)$$

This equation states that the wind speed at $z_{0,m}$ is zero but increases logarithmically with altitude. Figure 2.4.1 shows two examples of logarithmic wind profiles.

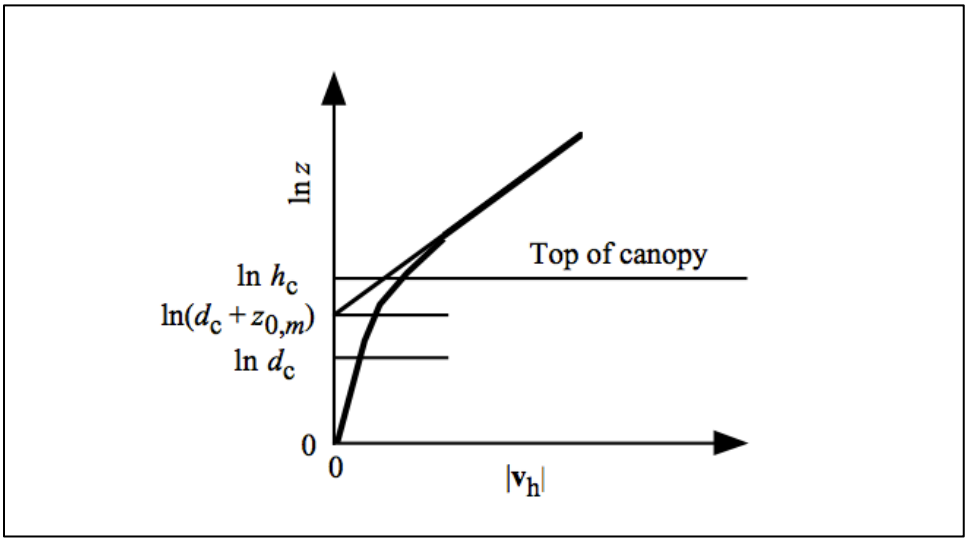

Figure 2.4.1 Relationship among d_c, h_c, and $z_{0,m}$.

The displacement height is found by plotting wind speed over a canopy versus lnz. The plotted wind speed is extrapolated to zero to obtain $d_c + z_{0,m}$. Different values of d_c are substituted into $d_c + z_{0,m}$ to estimate $z_{0,m}$. However, real wind profiles are often far from ideal. For some purposes, it is thus useful to fit observed wind profiles with analytical expressions (e.g., Archer and Jacobson 2003).

2.5 ASCE 7-10 Wind Code

Wind code has been discussed excessively in an amount of articles. Only some features associated with analysis in this work will be presented. More detailed information can be accessed with ASCE 7-10 Minimum Design loads for buildings and other structures.

2.5.1 Basic Wind Speed

Three-second gust speed at 33 ft (10 m) above the ground in Exposure C. The structure is assumed to be in Phoenix, where the 500 years base wind velocity, v=115mil/h=51m/s; Wind speeds correspond to approximately a 7% probability of exceedance in 50 years

(Annual Exceedance Probability = 0.00143, MRI = 700 Years).

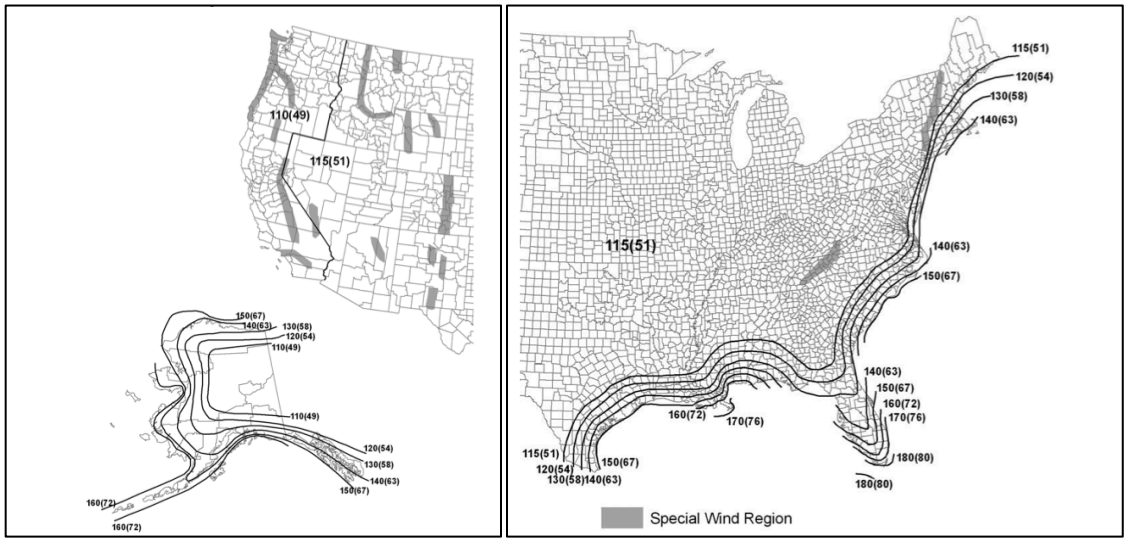

Figure 2.5.1 Basic Wind Speeds for Occupancy Category II Buildings and Other Structures Basic Wind Speeds for Occupancy Category II Buildings and Other Structures (ASCE 7-10)

2.5.2 Velocity Pressure

Natural frequency for the first mode is 0.376Hz. For flexible building, velocity pressure,

q_z, evaluated at height z shall be calculated by the following equation:

$$q_z = 0.613 K_z K_{zt} K_d V^2 \left(N/m^2\right) \qquad V \ \ in \ \ \ m/s \tag{2.5.1}$$

where

K_d = wind directionality factor,

K_Z = velocity pressure exposure coefficient, see

K_{zt} = topographic factor defined,

V = basic wind speed,

q_z = velocity pressure calculated using (2.5.1) at height z

q_h = velocity pressure calculated using (2.5.1) at mean roof height h.

2.5.3 Enclosed and Partially Enclosed Flexible Buildings

Design wind pressures for the MWFRS of flexible buildings shall be determined from the following equation:

$$p = qG_f C_p - q_i (GC_{pi})(lb/ft^2)(N/m^2) \tag{2.5.2}$$

where q, q_i, C_p, (GC_{pi}) and G_f (gust-effect factor) are as defined in ASCE code.

Recall (2.4.17) $\left|\bar{v}_h(z)\right| = \frac{u_*}{k}\left[\ln\left(\frac{z}{z_{o,m}}\right)\right]$

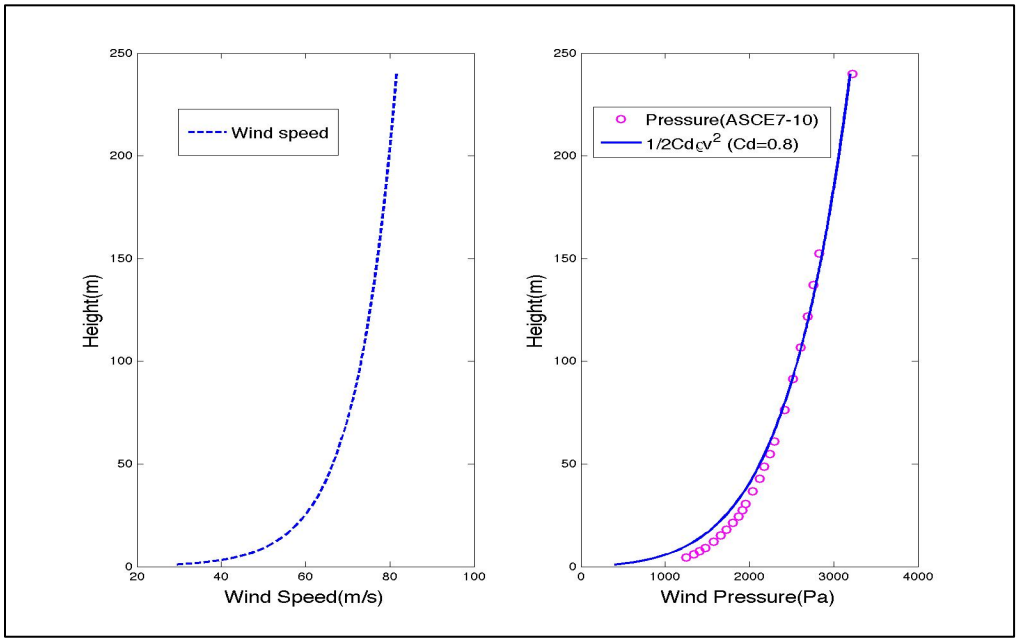

Figure 2.5.2 Wind Velocity Calculated with (2.4.17) and Wind Profiles in ASCE7-10

3 SQUARE PLANE DIAGRID STRUCTURAL SYSTEMS FOR TALL BUILDINGS

3.1 Introduction

With their structural efficiency as a varied version of the tubular systems, diagrid structures have been emerging as a new aesthetic trend for tall buildings. The effectiveness of diagonal bracing members in resisting lateral forces, for example wind load, provides the structure with higher resistance to earthquake and more economical advantage. Hearst Tower in New York City, designed by Sir Norman Foster, reportedly uses 21 percent less steel than a standard design.

Figure 3.1.1 Hearst Headquarters, New York

Most of the structural systems deployed for early tall buildings were steel frames with diagonal bracings of various configurations such as X, K, and chevron. Diagonals were generally embedded within the building cores, which were usually located in the interior of the building, since the aesthetic potential of diagonals was not appreciated once they were considered obstructive for viewing the outdoors.

The Shukhov tower in Polibino is the World's first diagrid hyperboloid structure designed in 1896 by Russian engineer and architect Vladimir Shukhov. The tower is located in the former estate of Yury Nechaev-Maltsov in the selo of Polibino in Lipetsk Oblast in Russia.

Figure 3.1.2 The World's First Diagrid Hyperboloid 37-meter Water Tower

The braced tubular structures were introduced in the late 1960s for the 100-story tall John Hancock Center in Chicago (Figure 1.1.1). The diagonals were located along the entire exterior perimeter surfaces of the building in order to maximize their structural

effectiveness and capitalize on the aesthetic innovation. This strategy is much more effective than confining diagonals to narrower building cores. Recently the use of perimeter diagonals for structural effectiveness and lattice-like aesthetics has generated renewed interest in architectural and structural designers of tall buildings.

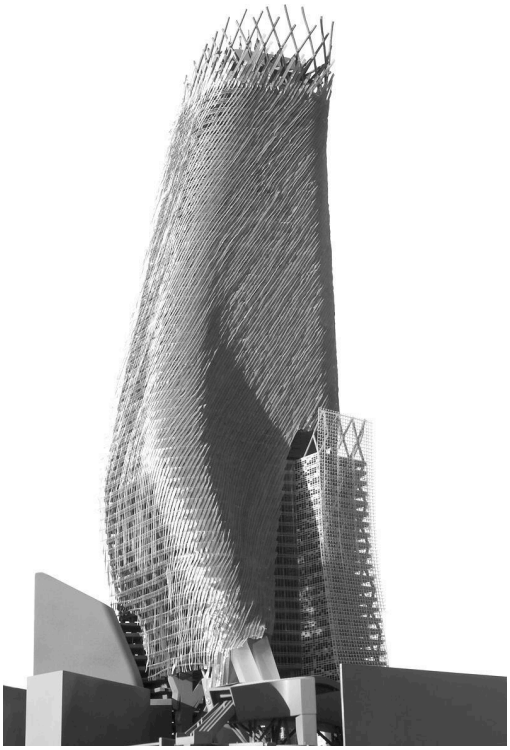

Figure 3.1.3 Morphosis' Phare Tower

Even though the supporting structural systems behind the free forms vary depending on the project-specific situations, diagrids are often employed as primary structures for free-form tall buildings as can be observed from Daniel Libeskind's Fiera Milano Tower and Morphosis' Phare Tower.

3.2 Diagrid System Structure

3.2.1 Geometry

With the rapid advancement of materials science and consequently produced higher strength materials, building structures are more often governed by stiffness requirements because of the lag in material stiffness versus material strength. This chapter presents a stiffness-based design methodology for the steel diagrid structural system for a square-plan tall building. Different from conventional design method primarily based on strength, the stiffness-based design methodology presented here is based on the structure's optimal deformation mode, which is dependent upon the height-to-width aspect ratio and grid geometry of the structure.

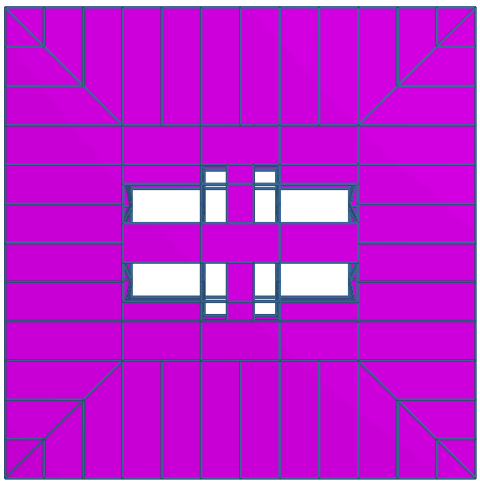

Figure 3.2.1 2-D Plan View

Figure 3.2.1 and Figure 3.2.2 shows 2D and 3D views of a typical candidate building. Geometric parameters for the buildings are listed in Table 3.2.1. Core bracings are configured to generate different fundamental periods in the x and y directions, while diagrids are configured symmetrically in both directions.

For the diagrid members, custom-made grade 50 steel pipes, varying diameters from 29 inches to 9 inches, are used. Their thickness varies from 3.5 inches for the 29-inch diameter pipes to 2 inches for the 9-inch diameter pipes. Box-shape grade 50 steel built-up sections of varying dimensions are used for the 16 core columns. Grade 36 W16 sections are selected for the beams, and W18 sections for the core bracings.

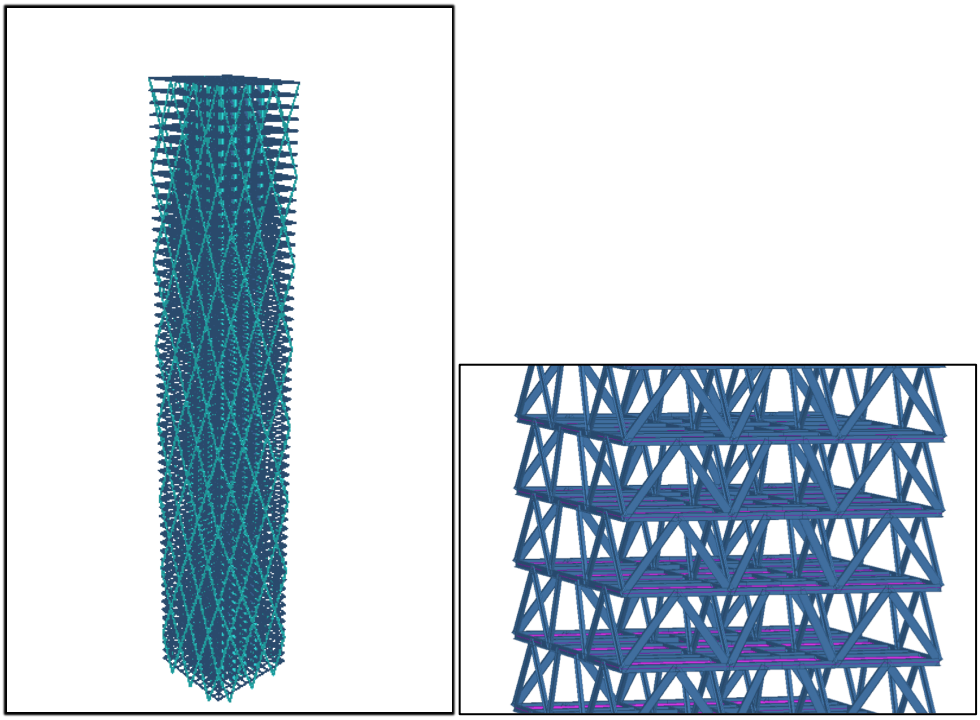

Figure 3.2.2 3-D Render View without Plates and Core Braces

The document SEI/ASCE 7-10 (Minimum Design Loads for Buildings and Other Structures) is used to establish the wind load. The buildings are assumed to be with category III, which implies that there is a substantial hazard to human life in the event of failure. Based on the code, the basic wind speed is 110mph. Lastly, 0.75% damping is assumed for the calculation of the gust effect factor. Member sizes were generated for the building with a diagrid angle of 69°.

Table 3.2.1 Geometric Parameters

Parameters	Magnitude (m)
Height	240
Width	36
Floor height	4
Plate thickness	0.125

3.2.2 Mode Shapes

Mode shapes of the building are calculated with Bentley STAAD.Pro and detailed figure are listed in Figure 3.2.3. First and second mode shape is slightly differed from each other since brace system at core part of the structure. Typically, only the first mode motion will be discussed in this work.

Table 3.2.2 Mode Shape Frequency

Modes	Frequency(Hz)	ω (rad/s)
1	0.392	2.46
2	0.393	2.47
3	1.46	9.16
4	1.49	9.36
5	1.53	9.61

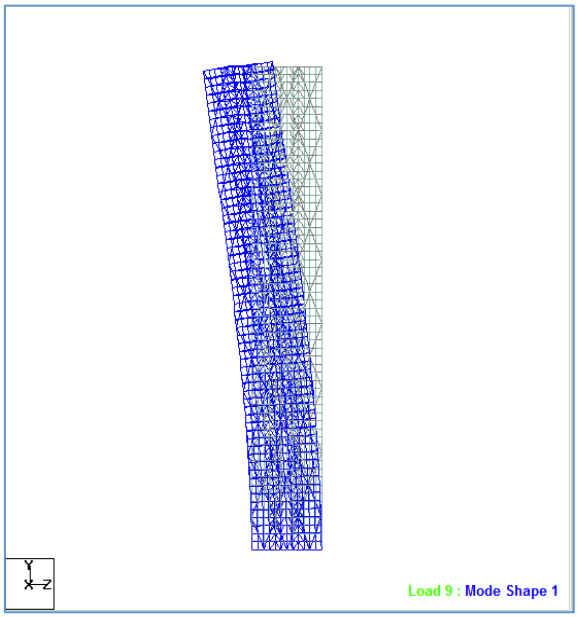

Figure 3.2.3 (a) First mode shape

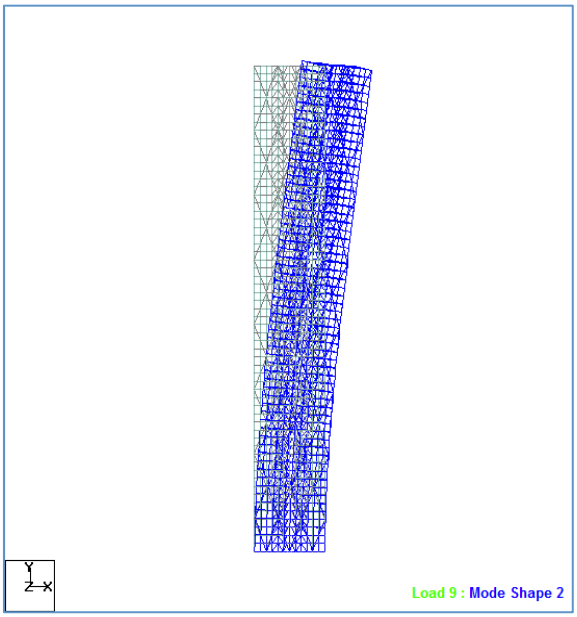

Figure 3.2.3 (b) Second mode shape

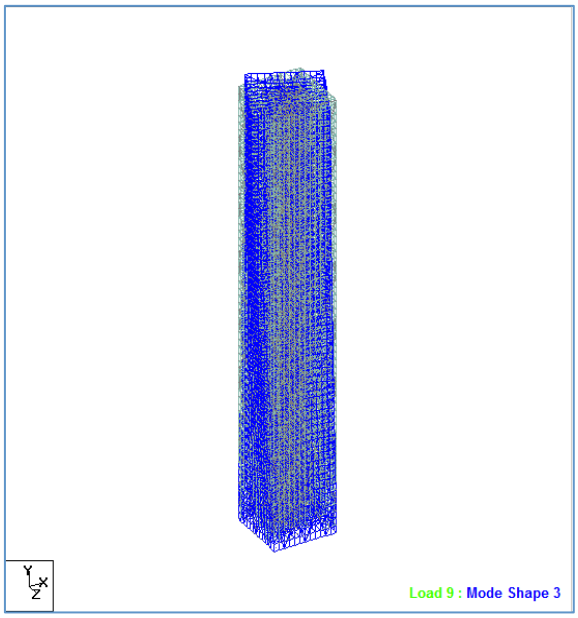

Figure 3.2.3 (c)Third mode shape

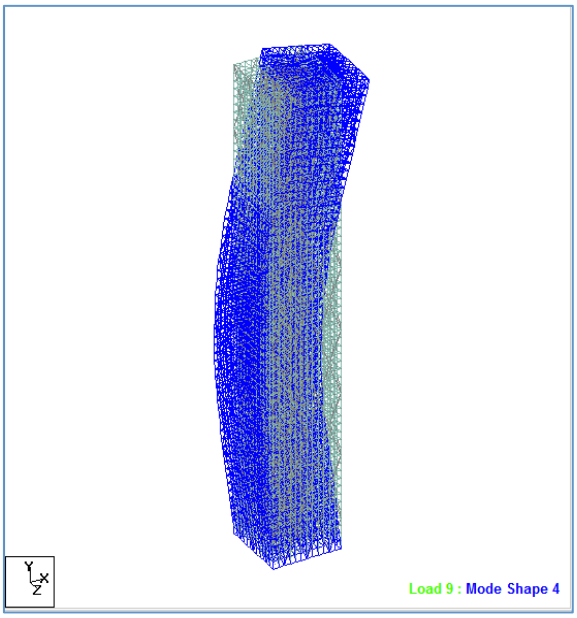

Figure 3.2.3 (d) Fourth mode shape

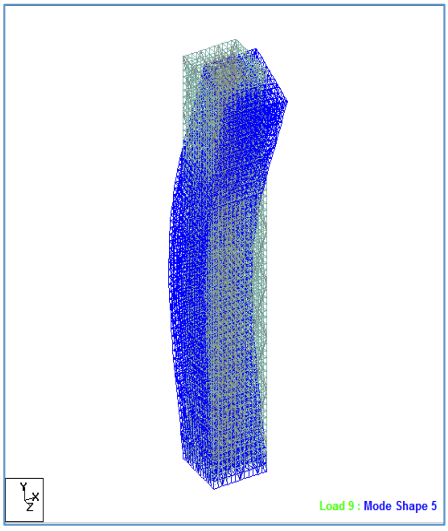

Figure 3.2.3(a)~(e) Mode Shapes of Strucure

3.3 Design Methodology

A diagrid structure is modeled as a vertical cantilever beam on the ground, and subdivided longitudinally into modules according to the repetitive diagrid pattern. Each module is defined by a single level of diagrids that extend over multiple stories. Figure 3.3.1 illustrates the case of an 8-story module. Depending upon the direction of loading, the faces act as either web planes (i.e., planes parallel to wind) or flange planes (i.e., planes perpendicular to wind). The diagonal members are assumed to be pin-ended, and therefore resist the transverse shear and moment through axial action only. With this idealization, the design problem reduces to determining the cross-sectional area of typical web and flange members for each module. Following the design methodology developed by Moon et al. (2007), member sizes for the modules can be computed using Equations (3.4.9) and (3.4.10) customized for each design case. In ASCE 7-10, ice load and seismic load are also important in design, but are not included within this work

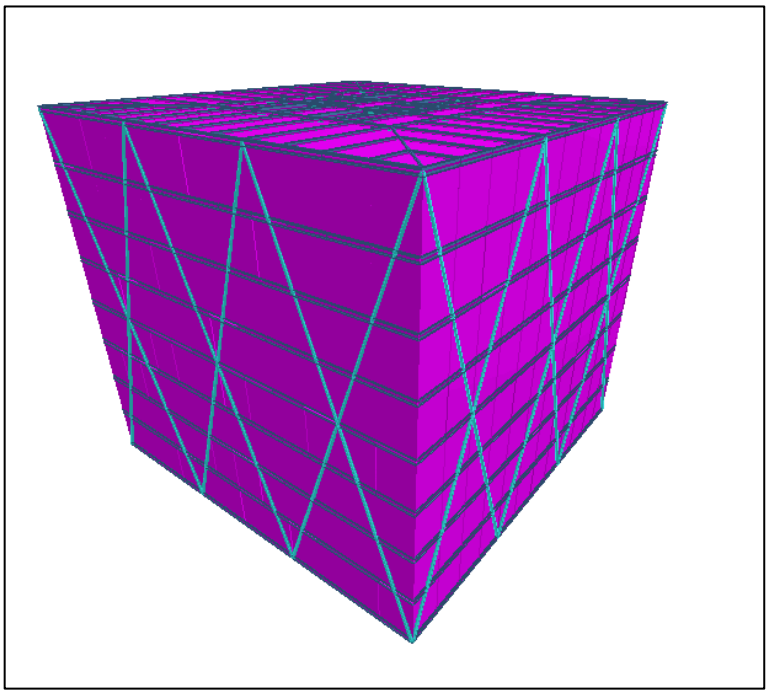

Figure 3.3.1 A typical 8 floor Module 3D View

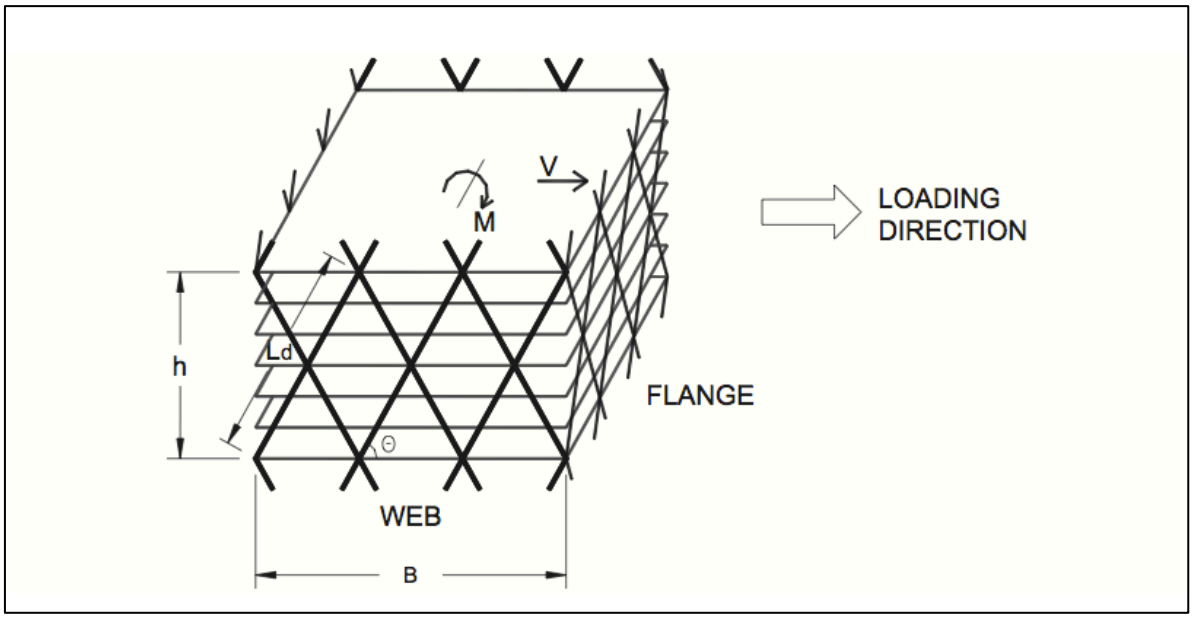

Figure 3.3.2 Diagrid Structure Module

The procedure begins by specifying the contributions to the total lateral displacement of the structure due to bending and shear deformation. This allocation is based on an assessment of the intrinsic attributes of diagrid structures and the behavioral characteristics of tall buildings related to their height to width ratio, and leads to the required values of shear and bending deformation. Simple equations which convert these required deformation values into cross-sectional areas for the diagrid members are derived.

This design methodology is applied to several diagrid structures of various heights and aspect ratios. Based on these studies, empirical guidelines for assessing the relative contribution of bending and shear deformation to the total lateral displacement of diagrid tall structures are derived. With this formula, the preliminary member sizing process is essentially automated.

3.3.1 Shear Stiffness and Bending Stiffness of Diagrid Structure

Model the building as a hollow section cantilever beam, and subdivide the beam longitudinally into modules according to the repetitive diagrid pattern. A single level of diagrids that extend over n stories defines each module. Figure 3.3.2 illustrates the case of a 6-story module. Depending upon the direction of loading, the faces act as either web or flange elements. The diagonal members are assumed to be pin-ended, and therefore to resist the transverse shear and moment through only axial action. With this idealization, the design problem reduces to determining the cross-sectional area of typical web and

flange members for each module. These quantities are established with a stiffness-based approach (Connor, 2003).

Referring both to Figure 8, the shear force *V* and bending moment *M* are expressed in terms of the relative displacement and rotation measures, D*u* and Db, for the module as

$$V = K_T \Delta u \tag{3.4.1}$$

$$M = K_B \Delta \beta \tag{3.4.2}$$

The motion measures are related to the transverse shear and bending deformation measures by

$$\Delta u = \gamma \cdot h \tag{3.4.3}$$

$$\Delta \beta = \chi \cdot h \tag{3.4.4}$$

where h is the height of the module and χ is the curvature. Applying the process described in Section 3.3 leads to the following expressions for the module stiffness measures:

$$K_T = 2N_w \left(\frac{A_{d,w} E}{L_d} \cos^2 \theta \right) \tag{3.4.5}$$

$$K_B = N_f \left(\frac{B^2 A_{d,f} E}{2L_d} \right) \sin^2 \theta \tag{3.4.6}$$

where N_W is the number of diagonals extending over the full height in one web plane, and Nf is a similar count for one flange plane.

Given *V* and *M*, one specifies the desired transverse shear and bending deformations, γ^* and χ^*, and determines the required stiffness using Equations (3.4.1) and (3.4.2).

$$K_T = \frac{V}{\gamma^* h} \tag{3.4.7}$$

$$K_B = \frac{M}{\chi^* h} \tag{3.4.8}$$

Lastly, substituting for the stiffness terms, one obtains expressions for the typical areas in the web and flange:

$$A_{d,w} = \frac{VL_d}{2N_w E_d h\gamma \cos^2\theta} \tag{3.4.9}$$

$$A_{d,f} = \frac{2ML_d}{N_f B^2 E_d \chi h \sin^2\theta} \tag{3.4.10}$$

E_d for Grade A50 steel is $3.447\times10^8 Pa$, L_d is the length of a single diagrid in Figure (3.4.2). θ in this design is 69.4°.

Since the diagonal members are assumed to be constant in a plane, one needs to consider loading in both directions in order to establish an upper board value for the areas.

3.3.2 Specifying the Shear and Bending Deformation Measures

Optimal design from a motion perspective corresponds to a state of uniform shear and bending deformation under the design loading. Uniform deformation states are possible only for statically determinate structures. Assuming the diagrid structure is modeled as a cantilever beam, the deflection at the top is given by

$$u(H) = \gamma^* H + \frac{\chi^* H^2}{2} \tag{3.4.11}$$

where $\gamma^* H$ is the contribution from shear deformation and $\frac{\chi^* H^2}{2}$ is the contribution from bending.

In order to specify the relative contribution of shear versus bending deformation, a dimensionless factor *s* is introduced, which is equal to the ratio of the displacement at the top of the structure due to bending and the displacement due to shear.

$$s = \frac{\frac{\chi^* H^2}{2}}{\gamma^* H} = \frac{H\chi^*}{2\gamma^*} \tag{3.4.12}$$

A shear beam is defined by s = 0. Tall buildings tend to have s ≈ 1. (Connor, 2003).

The maximum allowable displacement is usually expressed as a fraction of the total building height.

$$u(H) = \frac{H}{\alpha} \tag{3.4.13}$$

Noting Equations (3.4.11) and (3.4.12), Equation (3.4.13) expands to

$$u(H) = (1+s)\gamma h = \frac{h}{\alpha} \tag{3.4.14}$$

$$\gamma^* = \frac{1}{(1+s)\alpha} \tag{3.4.15}$$

$$\chi^* = \frac{2\gamma^* s}{H} = \frac{2s}{H(1+s)\alpha} \tag{3.4.16}$$

Typical values for α are in the neighborhood of 500. It remains to establish a value for *s*.

A dimensionless factor *f* is introduced, which is defined as the ratio of the strain in a web diagonal due to shearing action to the strain in a flange diagonal due to bending action.

Lateral loading produces both parts of strain. The strains can be expressed as

$$\varepsilon_{d,web} = \frac{\Delta u \cos\theta}{L_d} = \gamma \cos\theta \sin\theta \tag{3.4.17}$$

$$\varepsilon_{d,flange} = \frac{B\Delta\beta \sin\theta}{2L_d} = \frac{B}{2}\chi \sin^2\theta \tag{3.4.18}$$

The equation for f expands to

$$f = \frac{\varepsilon_{d,web}}{\varepsilon_{d,flange}} = \frac{2\gamma}{B\chi \tan\theta} \tag{3.4.19}$$

When a truss beam model is used to represent a tall building, the chords correspond to the columns of the building. These elements are required to carry both gravity and lateral loading, whereas the diagonals carry only lateral loading. Since the column force required by the gravity loading may be of the same order as the force generated by the lateral loading, the allowable incremental deformation in the column due to lateral loading must be less than the corresponding incremental deformation in the diagonal. Thus, *f* for braced-frame type tall buildings must be greater than 1. Typical values range from 3 for elastic behavior to 6 for inelastic behavior. However, in diagrid structures, the diagonals in both the web and flange planes are strained equally by the gravity loading. The diagonals at the interface between the web and flange are subjected to both shearing and bending deformation. Studies indicate that for optimally configured diagrid tall buildings having an aspect ratio (*H*/*B*) greater than about 5, *f* ranges from about 0·5 to 1. As the aspect ratio increases, the building tends to act more like a bending beam, and *f* decreases.

3.3.3 Minimum Weight

The methodology is applied to 60-story diagrid structures with an angle of 69.4°. The first step is to divide the structure into appropriate structural modules. For the 60-story building, an eight-story segment is used as the structural module. For each structural module, shear forces and bending moments are calculated using the code loadings described in Section 2.3. The 60-story building has an aspect ratio of about 7, and f was taken equal to 0.5. The corresponding value for s is about 6. Deformation measures were based on a maximum lateral displacement of $H/500$ = 0·48m. Member sizes for the modules were computed using the following equations customized for the eight-story module shown in Figure 3.3.1.

$$A_{d,w} = \frac{VL_d}{2N_w E_d h\gamma \cos^2\theta} = \frac{VL_d}{12E_d h\gamma \cos^2\theta} \tag{3.4.20}$$

$$A_{d,w} = \frac{VL_d}{N_f B^2 E_d \chi h \sin^2\theta} \approx \frac{2ML_d}{(6+2)B^2 E_d \chi h \sin^2\theta} \tag{3.4.21}$$

Adding one extra diagonal on each flange, resulting in $N_f \approx 6+2$, makes an estimate of the contribution of the diagonals on each web to the bending rigidity. (K.S. Moon.2007). Profiles of the required areas for the typical diagonals in the web and flange planes are plotted in Figure 3.3.1. Since the wind can blow in either direction, the role of a plane can be either a flange or a web. The building considered here has a square plan and the preliminary design value for the module is taken as the larger one of the two values.

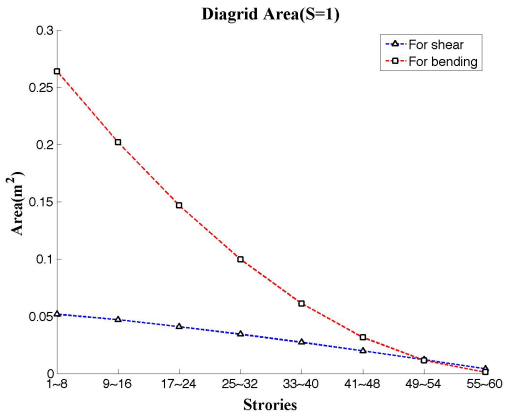
Diagrid Area(S=1)
For shear
For bending
Area(m2)
0.3
0.25
0.2
0.15
0.1
0.05
0
1~8
9~16
17~24
25~32
33~40
41~48
49~54
55~60
Strories

(a)

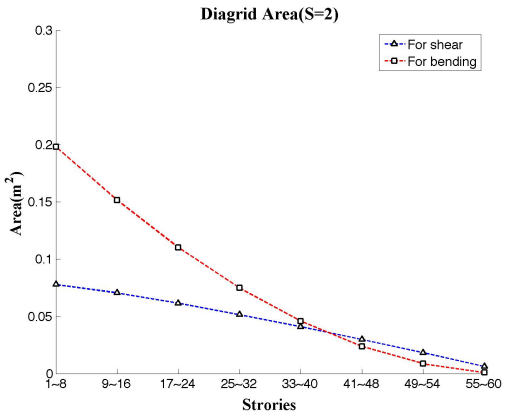
Diagrid Area(S=2)
For shear
For bending
Area(m2)
0.3
0.25
0.2
0.15
0.1
0.05
0
1~8
9~16
17~24
25~32
33~40
41~48
49~54
55~60
Strories

(b)

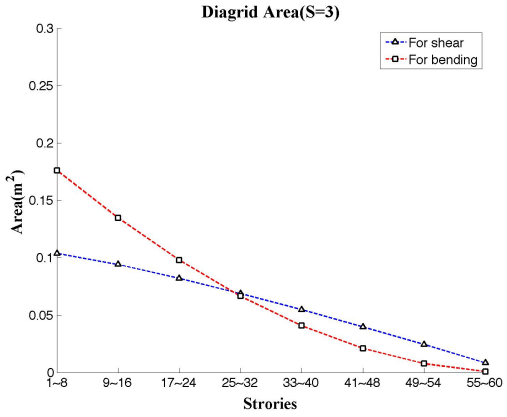
Diagrid Area(S=3)
For shear
For bending
Area(m2)
0.3
0.25
0.2
0.15
0.1
0.05
0
1~8
9~16
17~24
25~32
33~40
41~48
49~54
55~60
Strories

(c)

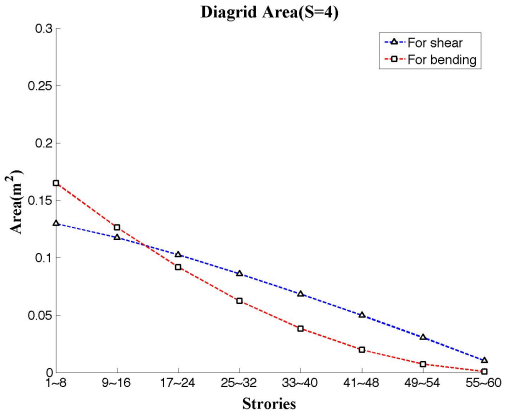
Diagrid Area(S=4)
For shear
For bending
Area(m2)
0.3
0.25
0.2
0.15
0.1
0.05
0
1~8
9~16
17~24
25~32
33~40
41~48
49~54
55~60
Strories

(d)

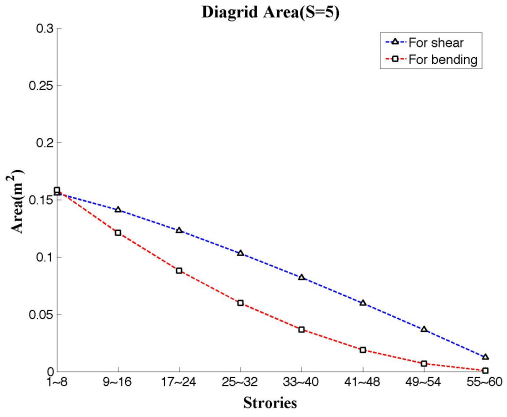
Diagrid Area(S=5)
For shear
For bending
Area(m2)
0.3
0.25
0.2
0.15
0.1
0.05
0
1~8
9~16
17~24
25~32
33~40
41~48
49~54
55~60
Strories

(e)

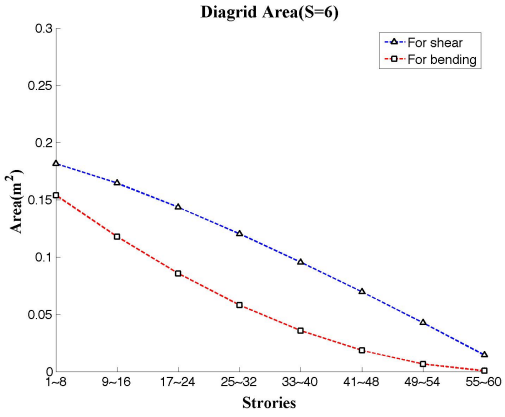
Diagrid Area(S=6)
For shear
For bending
Area(m2)
0.3
0.25
0.2
0.15
0.1
0.05
0
1~8
9~16
17~24
25~32
33~40
41~48
49~54
55~60
Strories

(f)

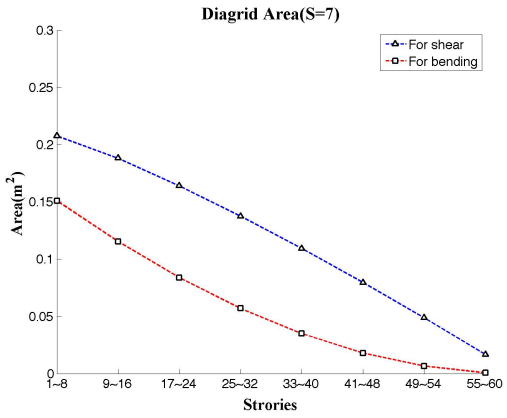

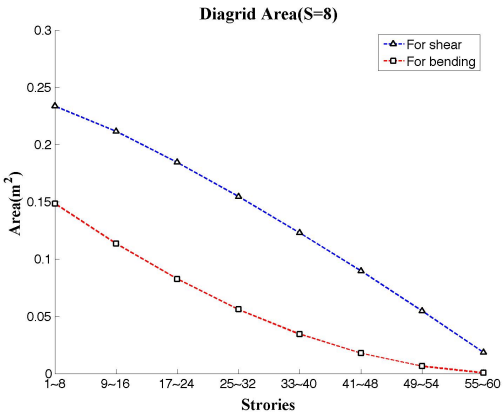

(g) (h)

Figure 3.3.1 (a)~(h) Member Sizes for Bending & Shear

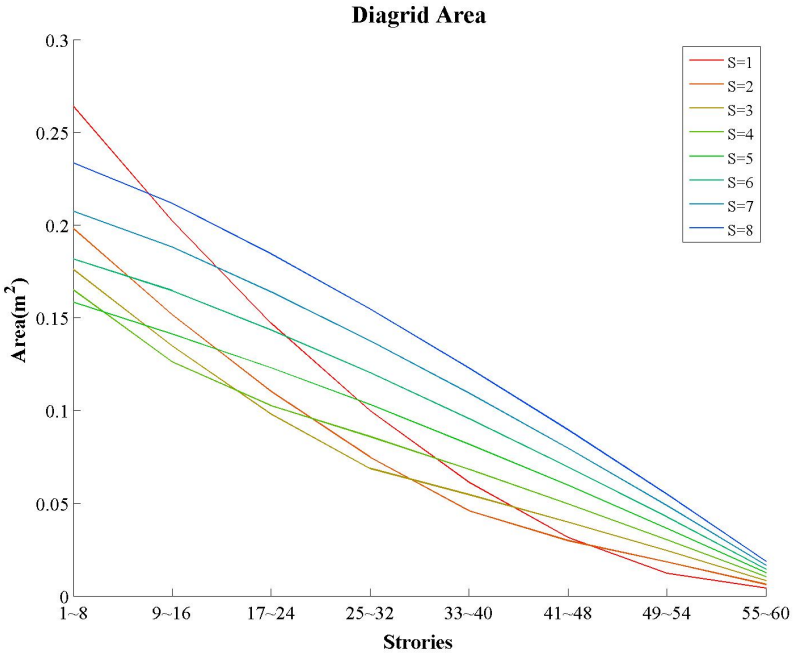

Figure 3.3.2 Diagrid Area Requirement for s=1~8

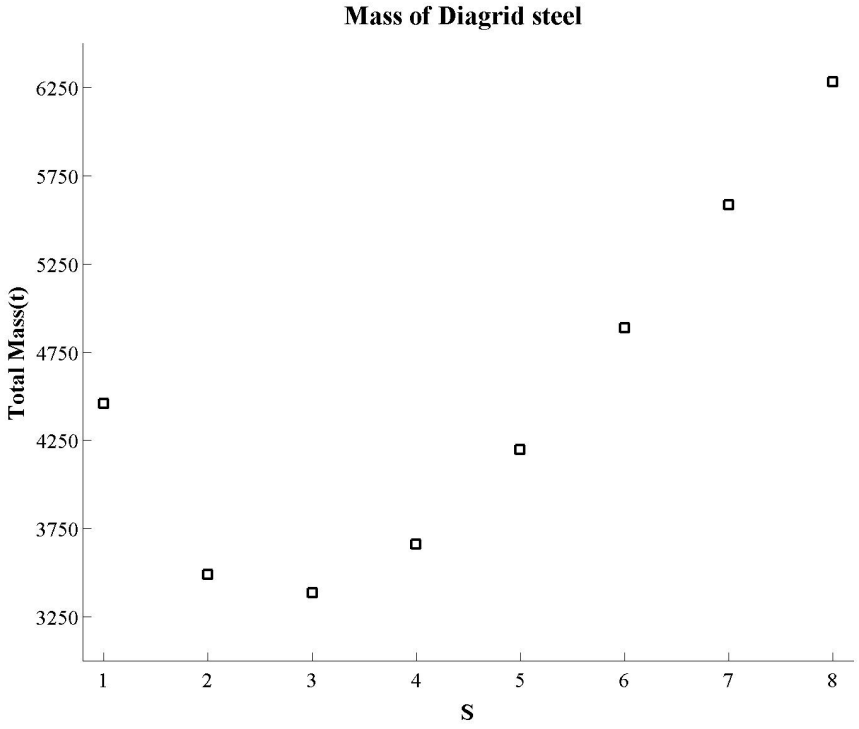

Figure 3.3.3 Diagrid Total Mass of Steel for s=1~8

Hence, S for a minimum weight of steel design should be 3. With S=3, computational results of Eqn. (3.4.20) and Eqn. (3.4.21) in comparison with diagrid area in design is listed in Figure 3.3.4. Maximum displacement at top of the structure is lower than 0.48m, since higher amount of steel is utilized on diagrids than computational results in consideration of load direction and its transverse direction.

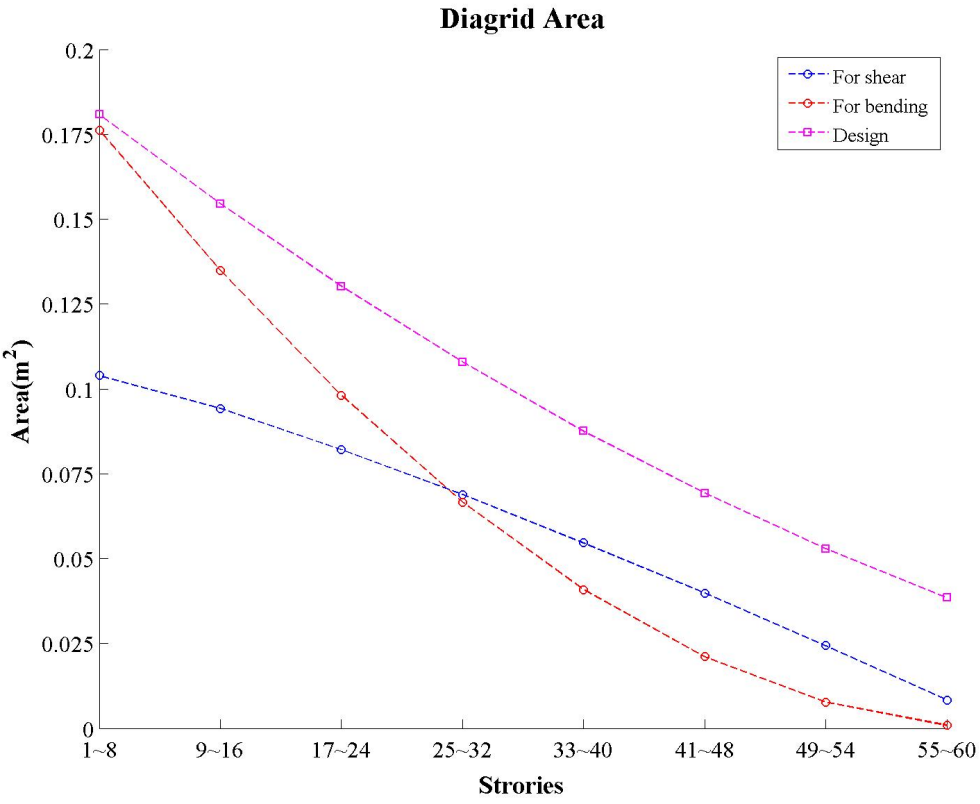

Figure 3.3.4 Diagrid Cross-section Area vs. Stories

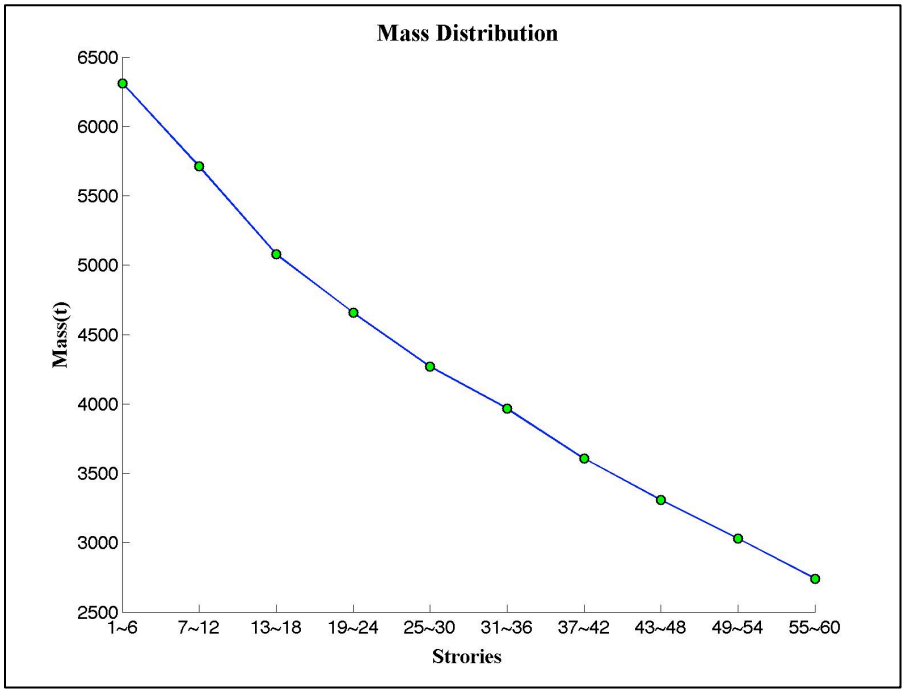

Figure 3.3.5 Structure Total Mass Distribution with Height

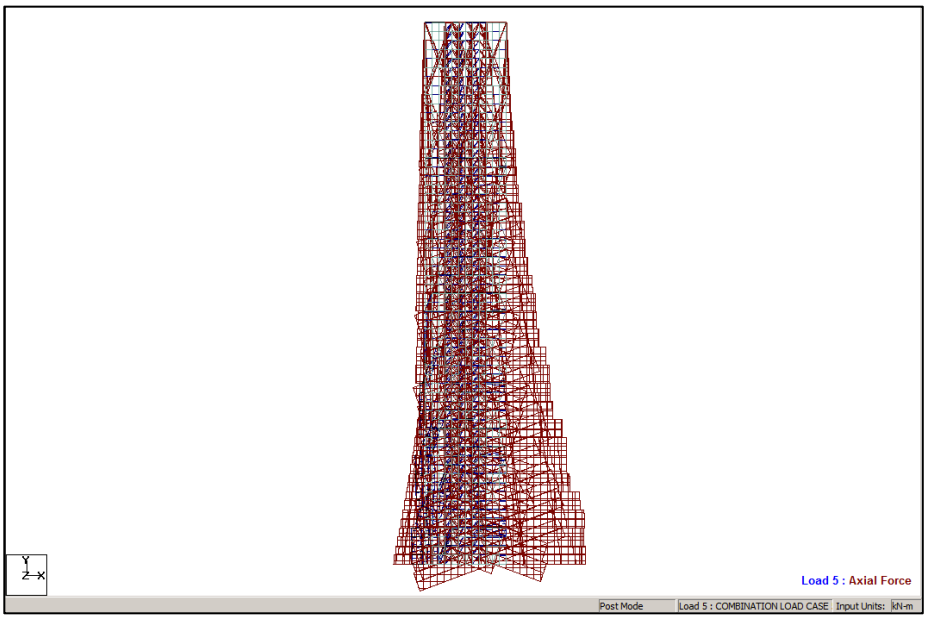

Figure 3.3.6 Axial Force of Beams under Wind Load and Self-weight

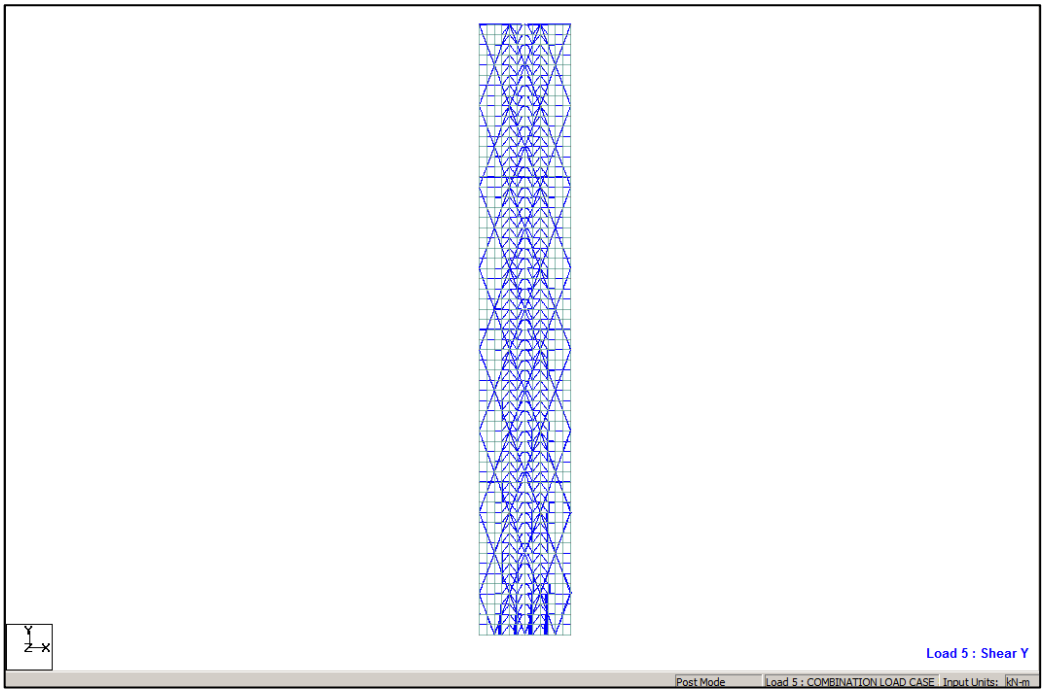

Figure 3.3.7 Shear Force of Beams under Wind Load and Self-weight

In Figure 3.3.6, the highest axial loads is on bottom ones of the diagrids, which is what expected, meanwhile the whole idea of the diagrid structure system, to put the brace at the surface of the building but not only in the core region. This will give us tremendous structural capacity material efficiency in withstanding horizontal loads like earthquake or wind load. As for the triangular members across stories fixed connections are not necessary as small enough shear forces in compare with axil force in Figure 3.3.7(plotted in the same scale as Figure3.3.6).

With wind load in positive x axial direction, which is the most likely direction to acquaint the first mode of the structure. Compression at lower level of leeward face of the structure is highest in this work, not from the negative wind pressure, which may dislocate plates outside of the building even with the highest wind velocity in the service

time of the structure. Compression and tensile stress in the beam is shown in Figure 3.3.8, while red is in compression and blue is for tension. Moreover, no steel member of the structure is with yielding or buckling issue.

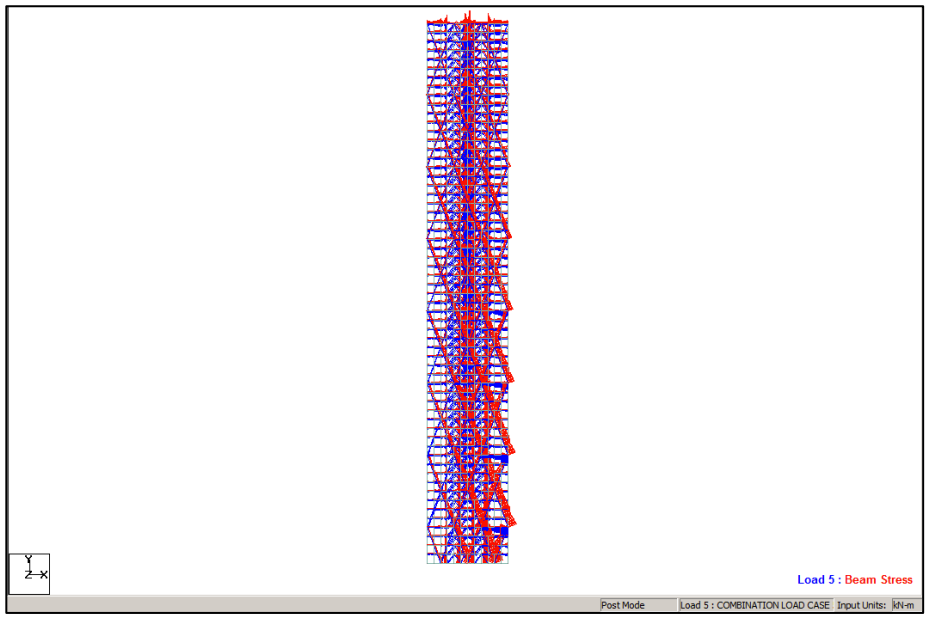

Figure 3.3.8 Stress of Beams under Wind Load and Self-weight

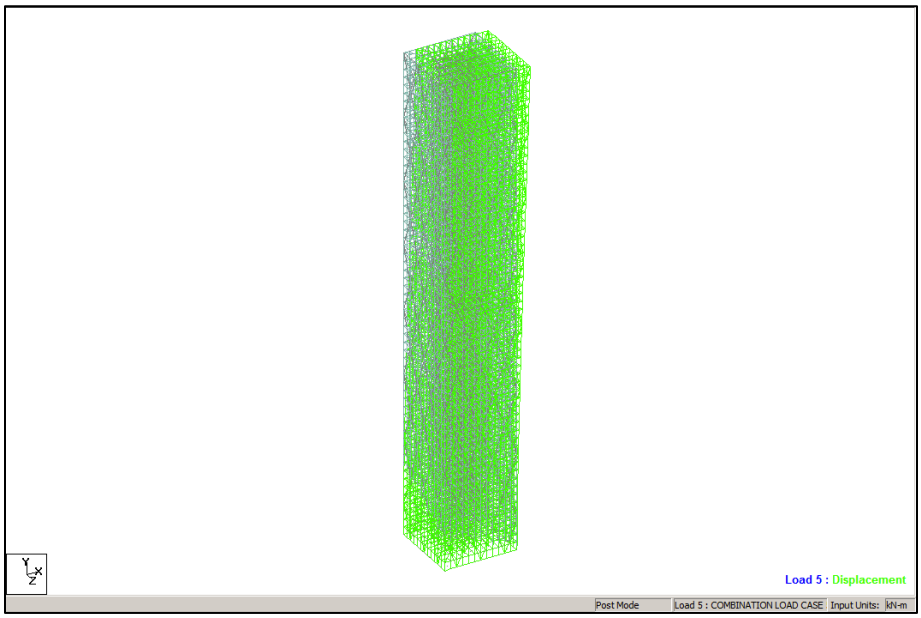

Figure 3.3.9 Displacement of Nodes under Wind load and Self-weight

With wind direction on x-axis direction, displacements of structure nodes are graphed with a scale factor.

3.4 Damping of the System

In dynamic analysis of structures damping plays an important role. The most effective way to treat damping within modal analysis framework is probably to treat the damping value as an equivalent Rayleigh Damping in form of

$$[C] = \alpha[M] + \beta[K] \tag{3.4.1}$$

in which

[C] = damping matrix of the physical system;

[M] = mass matrix of the physical system;

[K] = stiffness matrix of the system;

α and β are pre-defined constants.

The major advantage gained in converting the damping matrix into an equivalent Rayleigh damping lies in the fact that using orthogonal transformation a structure having n degrees of freedom can be reduced to n-number of uncoupled equations.

A system having multi-degrees of freedom, the equation of motion under externally applied time dependent force is given by

$$[M]\{\ddot{X}\} + [C]\{\dot{X}\} + [K]\{X\} = \{P_t\} \tag{3.4.2}$$

in which {Pt } force vector which is a function of time.

By orthogonal transformation, the above equation reduces to

$$\{\phi\}^T[M]\{\phi\}\{\ddot{\xi}\}+\{\phi\}^T[C]\{\phi\}\{\dot{\xi}\}+\{\phi\}^T[K]\{\phi\}\{\xi\}=\{\phi\}^T\{P_t\} \tag{3.4.3}$$

Eqn. (3.4.3), subsequently reduces to an n-uncoupled equations of the form

$$\{\ddot{\xi}_j\}+2\zeta_j\omega_j\{\dot{\xi}\}+\omega_j^2\{\xi_j\}=\{P_j(t)\} \tag{3.4.4}$$

in which

{ξ}= displacement of the structure in the transformed co-ordinate;

ζ = damping ratio in uncoupled mode;

ω=natural frequency of the system;

{P(t)}= modified force vector in transformed co-ordinate;

{φ}= normalized eigenvector of the system.

The above orthogonal transformation is valid only when the damping matrix is proportional i.e. it is some function of the mass and stiffness matrix [M] and [K]. It is for this reason that the damping in the form, shown in Eqn. (3.4.1), is advantageous as on orthogonal transformation the damping term in Eqn. (3.4.3) reduces to

$$\{\phi\}^T[C]\{\phi\}=\begin{bmatrix}\alpha+\beta\omega_1^2 & 0 & \cdots & 0\\ 0 & \alpha+\beta\omega_2^2 & \cdots & \vdots\\ \vdots & \vdots & \cdots & \vdots\\ 0 & \vdots & \cdots & \alpha+\beta\omega_n^2\end{bmatrix} \tag{3.4.5}$$

An iterative solution is possible and this can be obtained possibly from the best-fit values of α and β in a particular system. A method is described in the following through which

one can arrive at the unique values of Rayleigh coefficients and they will be valid also for systems having large degrees of freedom.

Computation of coefficients α and β for large systems

As it is shown in Eqn. (3.4.5), the orthogonal transformation of the damping matrix reduces the matrix [C] to the form

$$2\zeta_i\omega_i = \alpha + \beta\omega_i^2 \tag{3.4.6}$$

This, on simplification reduces to

$$\zeta_i = \frac{\alpha}{2\omega_i} + \frac{\beta\omega_i}{2} \tag{3.4.7}$$

One need not measure ζ_n, where n could be depended on the degree of freedom. What is relevant here is a first few modes for which there is a significant mass participation.

However, most of the civil engineering structures are usually designed to have a reasonable rigidity and would have a much higher value of the fundamental frequency, the term containing β will usually dominate. Moreover, considering the fact that the non-linear range is very small for normal structures it will not be unrealistic to assume that the damping ratio for each mode is linearly proportional to the frequency of the system.

The damping ratio thus obtained is given by

$$\zeta_i = \frac{\zeta_m - \zeta_1}{\omega_m - \omega_1}\left(\omega_i - \omega_1\right) + \zeta_1 \tag{3.4.8}$$

in which

ζ_i = damping ratio for the ith mode(for all $i \leq m$);

ζ_1 = damping ratio for the first mode;

ζ_m = damping ratio for the mth significant mode considered in the analysis;

ω_i = natural frequency for the ith mode;

ω_1 = natural frequency for the first mode;

ω_m = natural frequency for the mth significant mode considered for the analysis.

For structures having large degrees of freedom, it is only the first few modes, which contribute to the significant dynamic behavior. Now, how many modes will have a significant contribution can be ascertained from.

Based on an eigenvalue solution and modal mass participation result one can identify the significant modes (m) and follow the following procedure step by step as shown hereafter.

Select number of modes = 2.5 m and perform an eigenvalue analysis;

Select ζ_1, the damping ratio for the first mode of the system;

Select ζ_m, the damping ratio for the mth significant mode;

For intermediate modes i, where $1< i < m$, obtain ζ_i from Eqn. (3.4.8) based on linear interpolation;

For modes greater than m extrapolate the values based the expression

$$\zeta_i = \frac{\zeta_m - \zeta_1}{\omega_m - \omega_1}\left(\omega_{m+i} - \omega_m\right) + \zeta_1 \quad \text{where } m<i<2.5m \tag{3.4.9}$$

Select first set of data consisting of ζ_1, ζ_m, ω_1, ω_m

Based on the above sets of data obtain β from the equation

$$\beta = \frac{2\zeta_1\omega_1 - 2\zeta_m\omega_m}{\omega_1^2 - \omega_m^2} \tag{3.4.10}$$

Back-substituting the value of β in the expression

Simple rearrange Eqn. (3.4.6)

$$\alpha = 2\zeta_1\omega_1 - \beta\omega_1^2 \tag{3.4.11}$$

Select a second set of data consisting of ζ_1,$\zeta_{2.5m}$, ω_1, $\omega_{2.5m}$

Find out α and β based on eqns. (3.4.10) and (3.4.11).

Now one has the three sets of data

a) based on linear interpolation

b) based on data set ζ_1, ζ_m, ω_1, ω_m,

c) based on ζ_1,$\zeta_{2.5m}$, ω_1, $\omega_{2.5m}$,

d) obtain a fourth set of data based on the averages of b) and c) as mentioned above

Plot the four sets of data based on Eqn. (3.4.9) and check which data fits best with the linear interpolation curve for the first m significant modes.

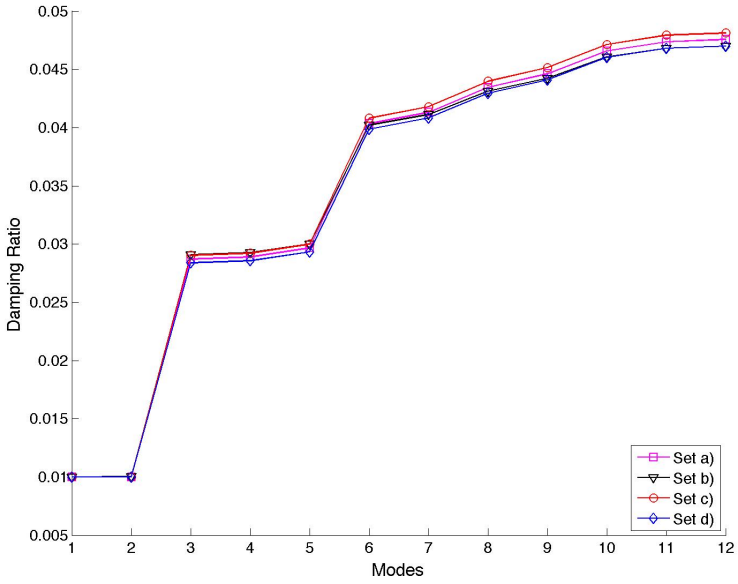

Figure 3.4.1 Variation of Damping Ratio

In Figure 3.4.1, assuming ζ_1=0.01, m=5, ζ_m=0.03, $\zeta_{2.5m}$=0.047, one can get $\alpha = 0.0122$, $\beta = 0.0063$.

Select the corresponding value of α and β as the desired value, which will give the incremental damping ratio based on Rayleigh damping.

3.4 Beam Theory

The basic idea behind beam theory is the hypothesis that cross sections that are plane before deformation remain plane after deformation, the so-called *plane-sections hypothesis*. (Although not often stated explicitly, an equally important assumption is that those plane sections do not distort in their own planes, either.)

Simplify wind loads into equivalent pressure alone height of the structure and replace hollow section beam with plan beam. With different basic wind velocities on the wind map of ASCE 7-10 varying from 40m/s to 87m/s, top displacements of 3-D finite element, Timoshenko and Euler beam model are shown in Figure 3.4.1. One might ask the top displacement has exceeded 0.48m as allowed. The length of beam is 240m, which ensures 'small displacement' assumption of beam theory.

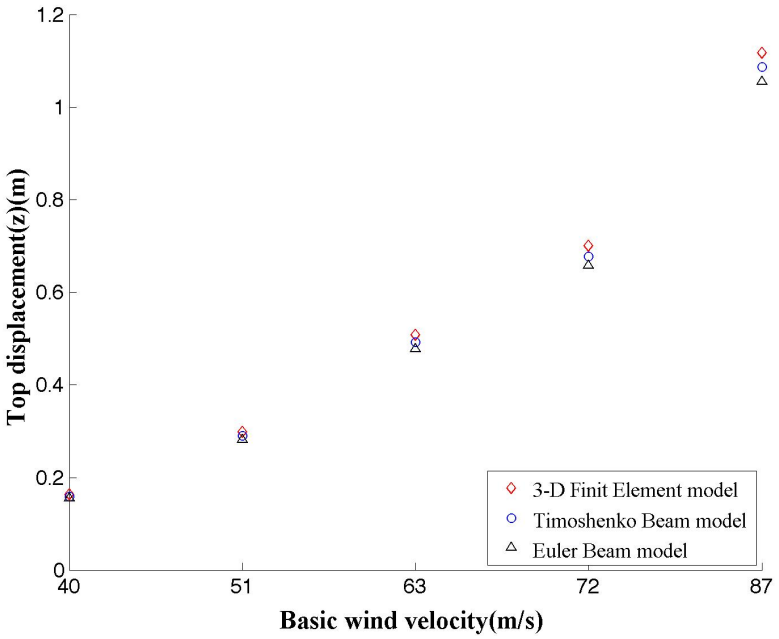

Figure 3.4.1 Top Displacements under Different Basic Wind Velocities

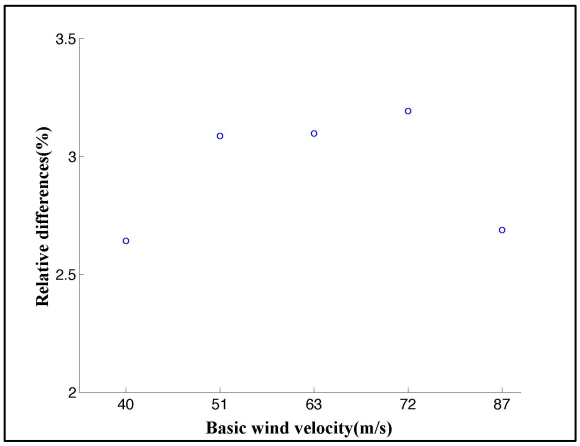

Figure 3.4.2 Relative Difference in Top Displacements between 3-D Finite Element and Timoshenko Beam Model

For a beam like structure in this work, a simulation of cantilever beam could considerably accurate result comparing to the frame and plate model as for the differences between 3-D to 2-D beam model is near around 3%.

3.5 Conclusion

A stiffness-based methodology for determining preliminary design sizes for the diagonals was introduced and applied to a representative set of steel buildings. Results for displacement and required steel tonnage demonstrate the practical usefulness of the proposed preliminary design method. Compared with a conventional strength-based iterative methodology, a stiffness-based methodology is more efficient for today's relatively light and flexible structures such as tall buildings, the design of which is in many cases governed by motion rather than strength.

As both x and z direction on plan has the possibility being the wind direction, section areas of the diagrid should be the greater value of between the bending and shear.

4 COMPUTATIONAL FLUID DYNAMIC AND FLUID STRUCTURE INTERACTION MODELING

4.1 Introduction

The mathematical model used for simulating the motion of air around the building incompressible finite mass model. A commercial computational fluid dynamics(CFD) code, Abaqus CFD, in Fulton School of Engineering eSpace High Performance Computing Lab is used for modeling. Brief outline of the numerical models applied will be discussed. More detailed derivations and programming technics can be found in Joel H. Ferziger (2002) and C.A.J Fletcher(1991). In saving the number of elements and avoiding internal influence of the structure, a hollow square cylinder are model as the same deflection resistance as the diagrid with descending mass and stiffness from bottom to top of the model. Fluid Structure Interact (FSI) of the fluid and structure model is also used here. Basic wind velocity is taken as 51m/s, which is the maximum wind load condition in designing the structure.

The onset flow for a wind-engineering model can be idealized as a horizontally-homogeneous turbulent boundary layer, with the flow being driven by a shear stress at the top boundary. The inlet profiles and boundary conditions appropriate for modeling the flow using the k-ε turbulence models are derived.

4.2 Theory of Computational Fluid Dynamics

4.2.1 Conservation Principles

Conservation laws can be derived by considering a given quantity of matter or control mass (CM) and its extensive properties, such as mass, momentum and energy. This approach is used to study the dynamics of solid bodies, where the CM (sometimes called the system) is easily identified. In fluid flows, however, it is difficult to follow a parcel of matter. It is more convenient to deal with the flow within a certain spatial region which is called a control volume (CV), rather than in a parcel of matter which quickly passes through the region of interest. This method of analysis is called the control volume approach.

The conservation law for an extensive property relates the rate of change of the amount of that property in a given control mass to externally determined effects. For mass, which is neither created nor destroyed in the flows of engineering interest, the conservation equation can be written:

$$\frac{dm}{dt} = 0 \tag{4.2.1}$$

On the other hand, momentum can be changed by the action of forces and its conservation equation is Newton's second law of motion:

$$\frac{d(mv)}{dt} = \sum f \tag{3.2.2}$$

where t stands for time, m for mass, v for the velocity, and f for forces acting on the

control mass. The fundamental variables will be intensive rather than extensive properties; the former are properties, which are independent of the amount of matter considered. Examples are density p (mass per unit volume) and velocity v (momentum per unit mass). If Φ is any conserved intensive property (for mass conservation, Φ = 1; for momentum conservation, Φ = v; for conservation of a scalar, Φ represents the conserved property per unit mass), then the corresponding extensive property can be expressed as:

$$\Phi = \int_{\Omega_{CM}} \rho\phi \, d\Omega \tag{4.2.3}$$

where Ω_{CM} stands for volume occupied by the CM.

The integral form of the mass conservation (continuity) equation follows directly from the control volume equation, by setting Φ= 1.

By applying the Gauss' divergence theorem to the convection term, transform the surface integral into a volume integral. Allowing the control volume to become infinitesimally small leads to a differential coordinate-free form of the continuity equation:

$$\frac{\partial \rho}{\partial t} + div\left(\rho \upsilon\right) = 0 \tag{4.2.4}$$

$$\frac{\partial \rho}{\partial t} + \frac{\partial\left(\rho u_i\right)}{\partial x_i} = \frac{\partial \rho}{\partial t} + \frac{\partial\left(\rho u_x\right)}{\partial x} + \frac{\partial\left(\rho u_y\right)}{\partial y} + \frac{\partial\left(\rho u_z\right)}{\partial z} = 0 \tag{4.2.5}$$

In our case, wind around a civil structure is considered as incompressible fluid as for relatively low wind speed.

4.2.2 The Navier-Stokes Equations

The numerical solution of any fluid flow problem requires the solution of the general equations of fluid motion, the Navier-Stokes and the continuity equations. Fluid flow problems are described mathematically by these equations, which are a set of coupled non-linear partial differential equations with appropriate boundary conditions. These equations are derived from Newton's Second Law and describe the conservation of momentum in the flow.

The general form of the three dimensional incompressible instantaneous Navier-Stokes equations are as follows, in Cartesian tensor form:

$$\frac{\partial(\rho u_i)}{\partial t} = -\frac{\partial(\rho u_i u_j)}{\partial x_j} - \frac{\partial P}{\partial x_i} + \frac{\partial}{\partial x_j}\left[\mu\left(\frac{\partial u_i}{\partial x_j} + \frac{\partial u_j}{\partial x_i}\right)\right] + F \tag{4.2.6}$$

$$\begin{pmatrix} acceleration \\ term \end{pmatrix} = -\begin{pmatrix} convection \\ term \end{pmatrix} - \begin{pmatrix} pressure \\ term \end{pmatrix} + \begin{pmatrix} viscosity \\ term \end{pmatrix} + \begin{pmatrix} body \\ force \end{pmatrix}$$

Full details of the derivation of these equations are referred to Young (1989).

4.2.3 Reynolds Number

For low speed laminar flows without heat transfer the equations detailed above can be used to describe the flow exactly. However, in turbulent flows the velocity components vary rapidly in both time and space and difficulties arise in the numerical discretization of the flow field as briefly described in Chapter 2. Furthermore, there is a major problem in

simply representing or modeling turbulence. This is due to the fact that turbulence is an extremely complex and little understood phenomena, which is defined by a number of highly complex mechanisms including irregularity, diffusivity, three dimensional vortices fluctuations and dissipation.

Fluid flow analysis aims to determine the relationship between pressure and flow velocity by solving Eqn. (4.2.6), which is subject to a geometric boundary condition, i.e., the interface surface at which a fluid contacts a solid object. As very small uneven roughness is unavoidably distributed over the whole surface of a solid object, fluid particles are completely captured on the solid surface due to the viscosity of the fluid. This property of fluids leads to a very important assumption such that a condition of zero fluid velocity (i.e., no slip) is achieved over the whole surface of a solid object.

The relative importance of the ratio of the inertial forces to the viscous forces for the flow conditions is quantified by taking L as the characteristic scale of flow and U as characteristic velocity of flow;

$$\frac{[F_{inertia}]}{[F_{viscous}]} = \frac{\rho \dfrac{U}{L/U}}{\mu \dfrac{U}{L^2}} = \frac{\rho UL}{\mu} = \mathrm{Re} \tag{4.2.7}$$

where Re represents a dimensionless number called the Reynolds number. If the Navier-Stokes Eqn. (4.2.6) is converted to a dimensionless form, it is well known that this dimensionless equation depends on only the Reynolds number. Thus, if Reynolds numbers are identical, an overall field containing every individual flow with a

geometrically similar boundary shape to each other can be regarded as being similar overall. In addition to increasing velocity, a greater density, a smaller viscosity, or a larger solid body size tend to increase the Reynolds number, thereby equally affecting the overall flow field. Accordingly, it can be said that the Reynolds number represents a dimensionless flow velocity.

4.3 Turbulence Models

The reader has previously been introduced to the Navier-Stokes equations (see section 4.2.2) and the necessity to make assumptions regarding these equations to allow for calculations of turbulent flow. Nonetheless, the procedure of time averaging these equations results in an additional set of terms, the Reynolds stresses, that have to be accurately represented in some way. Whereas the original instantaneous Navier-Stokes equations for laminar flow can be closed when the appropriate initial and boundary conditions are prescribed, the time-averaged equations unfortunately cannot. This is defined as the closure problem whereby further equations are required to tie the Reynolds stress tensor to the mean flow equations. The level of closure adopted refers to the number of supplementary transport equations required to achieve closure of the Reynolds equations. In this work, standard and Re-Normalization Group (RNG) $k-\varepsilon$ model models will be discussed.

The standard k-ε model (Launder and Spalding 1974) has two model transport equations, one for the turbulent kinetic energy of the flow, k and one for the dissipation rate of k, ε.

These values are used to define the velocity scale and the length scale, at any given point and time in the flow field, representative of large-scale turbulence as follows:

Velocity scale $$\vartheta = k^{\frac{1}{2}} \tag{4.2.8}$$

Length scale $$l = \frac{k^{\frac{3}{2}}}{\varepsilon} \tag{4.2.9}$$

where k=turbulent kinetic energy(TKE)

ε = the dissipation rate of turbulent kinetic energy

From this the eddy viscosity can be specified as follows:

$$\mu_t = C_\mu l \vartheta = \rho C_\mu \frac{k^2}{\varepsilon} \tag{4.2.10}$$

Inserting the Boussinesq hypothesis into the momentum equation yields

$$\frac{\partial \rho \overline{u_i}}{\partial t} = -\frac{\partial \rho \overline{u_j} \overline{u_i}}{\partial x_j} - \frac{\partial \overline{P}}{\partial x_i} + \frac{\partial}{\partial x_j}\left[u_{eff}\left(\frac{\partial \overline{u}_i}{\partial x_j} + \frac{\partial \overline{u}_j}{\partial x_i} \right) \right] \tag{4.2.11}$$

$$\mu_{eff} = \mu + \mu_t \tag{4.2.12}$$

The standard k-ε model equation is obtained by multiplication of the instantaneous Navier-Stokes equations by the appropriate fluctuating velocity components (i.e. x-component equation multiplied by u' etc.) and addition of all the results. This is followed by a repeat of this process on the time averaged Reynolds equations, subtraction of the two resulting equations and substantial re-arrangement yielding the equation for the turbulent kinetic energy k (Tennekes and Lumley 1972). It is also possible to develop similar transport equations, from the Navier-Stokes equations, for other turbulence

quantities including the rate of viscous dissipation ε. Nonetheless it should be noted that the energy dissipation equation is far more empirical and the modeling of terms is so severe that it is best to regard the entire equation as a model.

The standard k-ε model equations are (Eqn. (4.2.11)) as follows: Turbulent kinetic energy

$$\rho\frac{\partial k}{\partial t}+\rho\bar{u}_j\frac{\partial k}{\partial x_j}=\tau_{ij}\frac{\partial \bar{u}_i}{\partial x_j}-\rho\varepsilon+\frac{\partial}{\partial x_j}\left[\left(\mu+\mu_t/\sigma_k\right)\frac{\partial k}{\partial x_j}\right] \tag{4.2.13}$$

$$\begin{pmatrix}Increase\\rate\end{pmatrix}+\begin{pmatrix}Convective\\transport\end{pmatrix}=\begin{pmatrix}\text{Pr}oduction\\rate\end{pmatrix}-\begin{pmatrix}Destruction\\rate\end{pmatrix}+\begin{pmatrix}Diffusive\\transport\end{pmatrix}$$

Dissipation rate

$$\rho\frac{\partial \varepsilon}{\partial t}+\rho\bar{u}_j\frac{\partial \varepsilon}{\partial x_j}=C_{\varepsilon 1}\frac{\varepsilon}{k}\tau_{ij}-C_{\varepsilon 2}\rho\frac{\varepsilon^2}{k}+\frac{\partial}{\partial x_j}\left[\left(\mu+\mu_t/\sigma_k\right)\frac{\partial \varepsilon}{\partial x_j}\right] \tag{4.2.14}$$

$$\begin{pmatrix}Increase\\rate\end{pmatrix}+\begin{pmatrix}Convective\\transport\end{pmatrix}=\begin{pmatrix}\text{Pr}oduction\\rate\end{pmatrix}-\begin{pmatrix}Destruction\\rate\end{pmatrix}+\begin{pmatrix}Diffusive\\transport\end{pmatrix}$$

$\tau_{ij}=2\mu_t S_{ij}-\frac{2}{3}\rho k\delta_{ij}$ is Reynolds stress tensor and δ_{ij} the Kronecker delta.

$S_{ij}=\left(\frac{\partial \bar{u}_i}{\partial x_j}+\frac{\partial \bar{u}_j}{\partial x_j}\right)$

The various constants in the above equations are necessary due to the numerous simplifications made to the models and are derived from comprehensive data fitting to a wide range of turbulent flow fields (usually wind tunnel data).

To calculate the Reynolds stress tensor in the k-ε model a revised Boussinesq relationship is used from that shown

$$\tau_{ij}=-\rho\overline{u_i{}'u_j{}'}=\mu_t\left(\frac{\partial \bar{u}_i}{\partial x_j}+\frac{\partial \bar{u}_j}{\partial x_j}\right)-\frac{2}{3}\rho k\delta_{ij} \tag{4.2.15}$$

The effect of this extra term $-\frac{2}{3}\rho k\delta_{ij}$ added to the Boussinesq relationship is to make the term applicable to the normal Reynolds stresses as the standard hypothesis deals only with shear stresses. This term effectively allocates an equal third of the sum of the normal Reynolds stresses to each normal stress.

Re-Normalization Group (RNG) $k-\varepsilon$ model is a way to derive turbulence closure models was proposed by Yakhot and Orzag (1986). They applied Renormalisation Group theory to the Navier-Stokes equations and derived a two-equation k-ε model.

$$\rho\frac{\partial\varepsilon}{Dt}=\frac{\partial}{\partial x_m}\left(\frac{v_T}{\sigma_k}\frac{\partial k}{\partial x_m}\right)+2v_T E_{ij}E_{ji}-\varepsilon \tag{4.2.16}$$

$$C_{1RNG}=\frac{\eta\left(1-\frac{\eta}{\eta_o}\right)}{\left(1+\beta\eta^3\right)} \tag{4.2.17}$$

$$\eta=\left(\frac{P}{\mu_T}\right)^{\frac{1}{2}}\frac{k}{\varepsilon} \tag{4.2.18}$$

The remaining equations for this model are identical to the standard k-ε model.

4.4 Conclusion

In this chapter, some basic theories of Navier-Stokes Equations and turbulent models, which only related to computational fluid dynamics used in the next chapter, are introduced. For more details, readers are referred to J.H.Ferziger(1999) and Stephen(2000).

5 FLUID STRUCTURE INTERACTION

5.1 Fluid-structure Interaction (FSI)

For a structure degree based thesis, this work takes more concern on behavior of the structure rather than airflow around them. However, to fully review wind pressure pattern on the high-rise square-plane building, one has to do numerical analysis on fluid and dynamic effects it has on structure, which leads to the fluid-structure interaction problem.

In fluid-structure interaction (FSI) problems, one or more solid structures interact with an internal or surrounding fluid flow. FSI problems play prominent roles in many scientific and engineering fields, yet a comprehensive study of such problems remains a challenge due to their strong nonlinearity and multidisciplinary nature (Chakrabarti 2005, Dowell and Hall 2001, Morand and Ohayon 1995). For most FSI problems, analytical solutions to the model equations are impossible to obtain, whereas laboratory experiments are limited in scope; thus to investigate the fundamental physics involved in the complex interaction between fluids and solids, numerical simulations may be employed.

5.1.1 FSI Problem Formulation

Consider a computational domain, denoted by Ω, with an external boundary Γ. The domain includes the structural domain, $\overline{\Omega_S}$ and the fluid domain, $\overline{\Omega_f}$; i.e., $\Omega = \overline{\Omega_S} \cup \overline{\Omega_f}$. The fluid-structure interface is defined by $\Gamma_S = \overline{\Omega_S} \cup \overline{\Omega_f}$. See Figure 5.1.1 for illustration of the domains. For notational simplicity, adopt the tensor notation below.

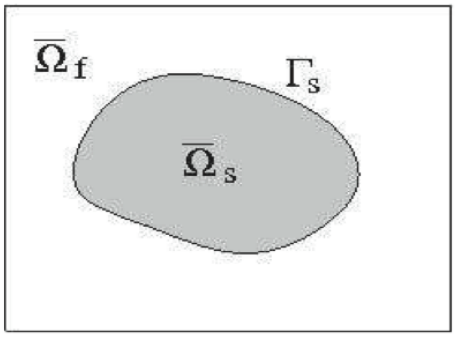

Figure 5.1.1 Schematic of the Fluid and Solid Domains in a FSI Problem.

The equations of motion for the fluid and structure may be expressed in the same index form, as a result of the D'Alembert's principle:

$$\rho v_i{}' - \sigma_{ij,j} + f_i = 0 \tag{5.1.1}$$

where f_i is the body force, such as gravity. Specifically, in the structural domain, the equation is written as

$$\rho^s \dot{v}_i^s - \sigma_{ij,j}^s + f_i^s = 0 \qquad in \ \ \overline{\Omega}_s \tag{5.1.2}$$

where the superscript, s, denotes the quantity associated with the structure. Note that the velocity, v_i^s, is the material (or total) time derivative of the displacement field u_i^s, i.e., $v_i^s = \dot{u}_i^s$. Eqn. (5.1.2) is usually given in the Lagrangian description. The first two terms in Eqn. (5.1.2) are associated with inertia and internal stresses, respectively. For example, for linear elastic materials, the structural stress follows the linear Hooke's law; i.e.,

$$\sigma_{ij}^s = \lambda \delta_{ij} \varepsilon_{ll} + 2G\varepsilon_{ij} \tag{5.1.3}$$

where the structural stress σ_{ij}^s is a function of the strains, ε_{ij}, and the Lame constants λ and G, which are defined by

$$\varepsilon_{ij} = \frac{1}{2}\left(u_{i,j} + u_{j,i}\right) \tag{5.1.4}$$

$$G = \frac{E}{2(1+\upsilon)} \tag{5.1.5}$$

$$\lambda = \frac{E\upsilon}{(1+\upsilon)(1-2\upsilon)} \tag{5.1.6}$$

where E and ν are the Young's modulus and the Poisson's ratio, respectively. In the fluid domain, the equation is given by

$$\rho^f \dot{v}_i^f - \sigma_{ij,j}^f + f_i^f = 0 \quad in \quad \overline{\Omega}_f \tag{5.1.7}$$

which is usually represented by the Eulerian description. Thus, in the inertia term, one has

$$\dot{v}_i^f = \frac{dv_i^f}{dt} = \frac{\partial v_i^f}{\partial t} + v_j^f v_{i,j}^f \tag{5.1.8}$$

Assuming that the incompressible Newtonian fluid model is used here, the fluid stress, σ_{ij}^f, is then given by

$$\tau_{ij} = 2\mu\left(e_{ij} - \frac{\delta_{ij}e_{kk}}{3}\right)$$

$$e_{ij} = v_{j,i}^f + v_{i,j}^f$$

$$\sigma_{ij}^f = -p\delta_{ij} + \tau_{ij} \tag{5.1.9}$$

Note that p is the static pressure, which may be viewed as the necessary force to enforce the incompressibility condition, $v_{i,i}^f = 0$.

To maintain the no-slip condition along the fluid-structure interface Γs, the following Dirichlet and Neumann conditions can be imposed,

$$v_i^s = v_i^f \quad on \quad \Gamma_s \tag{5.1.10}$$

$$\sigma_{ij}^s n_i = \sigma_{ij}^f n_i \quad on \quad \Gamma_s \tag{5.1.11}$$

Eqn. (5.1.11) is in fact the differentiation of the displacement condition that both fields share the same interface,

$$x_i^s = x_i^f \quad on \quad \Gamma_s \tag{5.1.12}$$

For an interface profile that is smooth in time and space, some FSI methods consider Eq. (5.1.12) as the Dirichlet constraint, instead of Eqn. (5.1.10).

As mentioned before, FSI numerical techniques can be categorized into two classes; i.e., methods with conforming and non-conforming meshes. These in turn depend upon the procedure used to enforce the transmission conditions, Eqns. (5.1.10)-(5.1.12). The conforming- mesh methods track the motion of the interface and enforce Eqns. (5.1.11) and (5.1.12) on the interface explicitly, thus requiring mesh update. The conforming-mesh method provides a convenient framework to incorporate the partitioned approach. The non-conforming mesh methods, most notably, the immersed boundary method (Peskin 1977, 2002), enforce the Dirichlet condition, Eqn. (5.1.10) instead. The non-conforming mesh methods can be derived from the theorem of Lagrange multipliers (Haug 1992), where the Lagrange multipliers in most cases appear as source (or, forcing) terms in the fluid equation. Thus, in these methods, computation of the Lagrange multipliers is essential and directly affects the accuracy of the fluid and solid solutions.

In Abaqus, Arbitrary Lagrangian–Eulerian Methods(J. Donea et al) is used which is discussed in next session.

5.1.2 Arbitrary Lagrangian–Eulerian Methods

The numerical simulation of multidimensional problems in fluid dynamics and nonlinear solid mechanics often requires coping with strong distortions of the continuum under consideration while allowing for a clear delineation of free surfaces and fluid–fluid, solid–solid, or fluid–structure interfaces. A fundamentally important consideration when developing a computer code for simulating problems in this class is the choice of an appropriate kinematical description of the continuum. In fact, such a choice determines the relationship been the deforming continuum and the finite grid or mesh of computing zones, and thus conditions the ability of the numerical method to deal with large distortions and provide an accurate resolution of material interfaces and mobile boundaries.

The algorithms of continuum mechanics usually make use of two classical descriptions of motion: the Lagrangian description and the Eulerian description; see, for instance, (Malvern, 1969). The arbitrary Lagrangian – Eulerian (ALE) description, which is the subject of the present chapter, was developed in an attempt to combine the advantages of the above classical kinematical descriptions, while minimizing their respective drawbacks as far as possible.

5.2 Horizontally Homogenous Boundary Layer

For a number of years eddy-viscosity turbulence models have dominated industry use of CFD; as noted by Bradshaw (1999) “it is so obvious that stress-transport models are more realistic in principle than eddy viscosity models that the improvements they give are very disappointing”. However, it is shown that the use of an eddy-viscosity based model of a HHTBL can lead to spurious over-prediction of the pressure on windward faces of bodies in the boundary layer, whereas a Reynolds-stress transport model does not exhibit this undesirable behavior, suggesting that use of the latter deserves consideration.

Richards and Hoxey (1993) modeled a HHTBL by proposing velocity and turbulence property profiles, together with the associated boundary conditions, for the standard *k*-*ε* turbulence model.

5.3 Boundary Conditions for a Horizontally Homogeneous Boundary Layer

Richards and Hoxey (1993) modeled a HHTBL by proposing velocity and turbulence property profiles, together with the associated boundary conditions, for the standard k-ε turbulence model and showing that these satisfied horizontal homogeneity provided the model constants satisfied particular relationships.

An alternative approach is to derive the profiles directly from the conservation and equilibrium equations associated with a particular turbulence model for a HHTBL. The turbulence model has chosen its own value for von Kármán’s constant κ. The usual k-ε turbulence model constants $C\varepsilon1=1.44$, $C\varepsilon2= 1.92$, $C\mu= 0.09$ and $\sigma\varepsilon=1.3$ give

$$\kappa = \sqrt{(C_{\varepsilon 2} - C_{\varepsilon 1})\sigma_\varepsilon \sqrt{C_\mu}} = 0.4327$$

With the standard k-ε model and a rough wall with U=0 at z=z_0 these yield:

$$U = \frac{u_* \ln(z / z_o)}{\sqrt{(C_{\varepsilon 2} - C_{\varepsilon 1})\sigma_\varepsilon \sqrt{C_\mu}}} = \frac{u_* \ln(z / z_o)}{\kappa} \tag{5.4.1}$$

$$k = \frac{u_*^2}{\sqrt{C_\mu}} \tag{5.4.2}$$

$$\varepsilon = \frac{u_*^3}{\kappa z} \tag{5.4.3}$$

where u_* is the friction velocity associated with the constant shear stress

$$\tau_{xz} = \rho u_*^2 \tag{5.4.4}$$

The form of Eqn. (5.4.1) only differs from that given by Richards and Hoxey in terms of the definition of the height at which the velocity is zero. The requirement that the shear stress τ_{xz} is constant requires that the eddy viscosity varies linearly with the height

$$u_T = C_u \rho \frac{k^2}{\varepsilon} = \rho u_* \kappa z = C_\mu^{\frac{1}{4}} \rho k^{\frac{1}{2}} \kappa z \tag{5.4.5}$$

To implement such a profile the shear stress is imposed at the upper boundary of the domain, a zero flux condition is set for k, and the flux of ε across the boundary is prescribed as,

$$\frac{\mu_T}{\sigma_\varepsilon} \frac{d\varepsilon}{dz} = -\frac{\rho u_*^4}{\sigma_\varepsilon z} \tag{5.4.6}$$

A similar analysis for the k-ω turbulence model (Wilcox, 1993) yields essentially the same profiles for U and k, however with the standard constants $C_\mu=\beta'=0.09$, $\alpha=5/9$, $\beta=0.075$ and $\sigma_\omega=2$ the effective von Kármán's constant is given by

$$\kappa = \sqrt{\frac{(\beta - \alpha\beta')\sigma_\omega}{\sqrt{\beta'}}} = 0.408 \tag{5.4.7}$$

The specific dissipation rate, ω, profile is given by

$$\omega = \frac{u_*}{\sqrt{\beta'}\kappa z} \tag{5.4.8}$$

To implement the model similar boundary conditions are imposed at the upper boundary, with the flux of ω being prescribed as

$$\frac{\mu_T}{\sigma_\omega}\frac{d\omega}{dz} = -\frac{\rho u_*^2}{\sqrt{\beta'}\sigma_\omega z} \tag{5.4.9}$$

To implement these models in program the boundary condition at the top of the domain can be imposed as a free-slip wall, with a specified shear stress and a flux term for ε or ω as given in Eqn.(5.4.6) and Eqn.(5.4.9) as appropriate. All other turbulence scalars have a zero gradient boundary condition. Previous versions of Abaqus did not allow this shear stress boundary condition, but the shear stress and ε gradient could be imposed by creating a sub-domain one cell thick at the top boundary and prescribing a volume momentum source to drive the flow, and a volume sink term for ε or ω.

For a HHTBL, modeled using the k-ε turbulence model, the analytic solution for the layer is given above in Eqn. (5.4.3). For such a layer k is constant, and so the turbulence production P_k must equal the dissipation throughout the flow, since there is no vertical

component of diffusion or convection. Using the profile for velocity given in Eqn. (5.4.3), its derivative with respect to height, the definition of μ_T in Eqn. (5.4.5), and comparing with the profile of ε in Eqn. (5.4.3) the flow is indeed in equilibrium,

$$P_k = \mu_T \left(\frac{dU}{dz} \right)^2 = \frac{\rho u_*^3}{\kappa z} = \rho \varepsilon \tag{5.4.10}$$

Whilst this is true for the analytic solution, it is not necessarily the case for its discrete form. Hargreaves and Wright (2007) also noted a spike in turbulence kinetic energy in the second cell above the ground and suggested it was a feature of the *k*-ε model. However, it appears that this phenomenon is more related to the discretization process used in calculating the production term than the particular turbulence model. Conventionally P_k is calculated using the cell centered value for μ_T, and cell centered differences for the gradient of U, whilst the shear stresses in the momentum equations are calculated using face centered differences.

Consider a finite volume cell P, in a mesh of constant spacing Δz. For a HHTBL layer τ_{xz} is constant, and so the stresses at the north and south faces of the cell can be used to give the velocities in the neighboring cells N and S.

The estimate for the turbulence production,

$$P_k = \mu_T \left(\frac{dU}{dz} \right)^2 \approx \mu_T \left(\frac{\mu_N - \mu_s}{2\Delta z} \right)^2 = \frac{\rho u_*^3}{\kappa z} \alpha \tag{5.4.11}$$

$$\alpha = \left(\frac{1}{1 - \left(\Delta z / 2z \right)^2} \right)^2 \tag{5.4.12}$$

From this it can be seen that P_k does not equal $\rho\varepsilon$ as is required for equilibrium, but instead exceeds it by a factor α which increases as the ratio $\Delta z/z$ increases. For a constant mesh spacing α is at a maximum approaching the wall, as will k. The TKE of 51m/s fluid flow is shown in Figure 5.3.1, for a HHTBL calculated in section 2.4. For the near wall cell the values of P_k and ε are fixed by the wall function, but for the second interior node where k is calculated using the conservation equation, k reaches a local maximum.

To prevent this anomalous spike in the value of k the production may be recast into a form that uses the shear stresses at the north and south cell faces,

Since τ_{xz} is a constant across the boundary layer (and using Eqn. (5.4.5) for μ_T),

$$P_k = \frac{2\rho^2 u_*^4}{2\rho u_* \kappa z} = \frac{\rho u_*^3}{\kappa z} = \rho\varepsilon \tag{5.4.13}$$

and so the boundary layer can be seen to be in equilibrium.

Table 5.3.1 Wind Profile of Turbulence Model

Wind velocity (m/s)	Turbulent kinetic energy (m^2/s^2)	Dissipation rate near ground	Dissipation rate
40	35.65	23.59	1.05
51	57.82	48.9	2.18
63	88.23	92.18	4.11
72	115.23	137.6	6.13
87	168.25	242.75	10.81

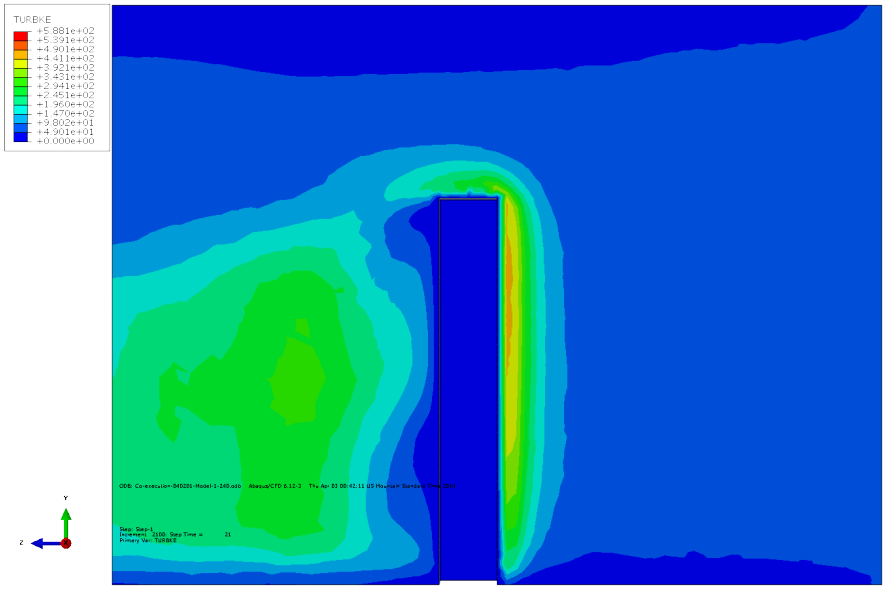

Figure 5.3.1 Turbulent Kinetic Energy Distribution (Center Cut View)

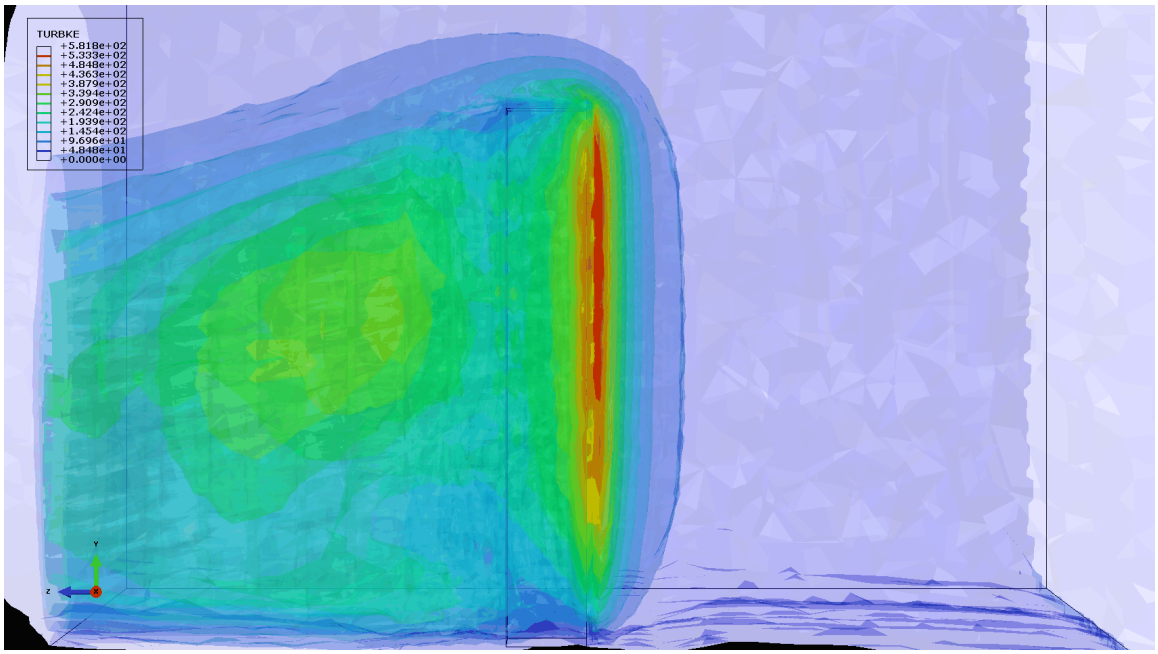

Figure 5.3.2 Turbulent Kinetic Energy Isolate Faces

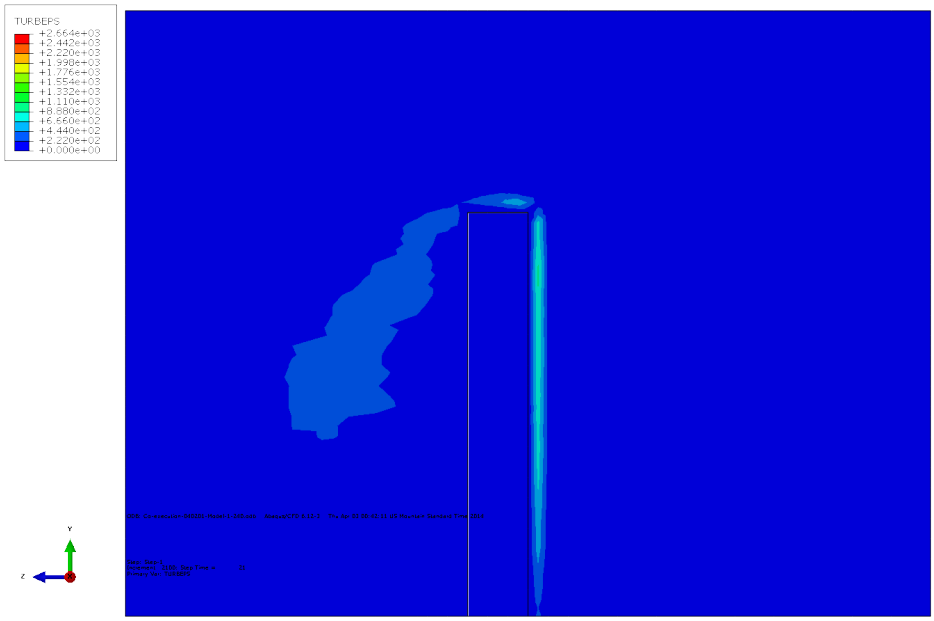

Figure 5.3.3 Dissipation Rate (Side Wall Cut View)

5.4 Numerical Analysis Tactics

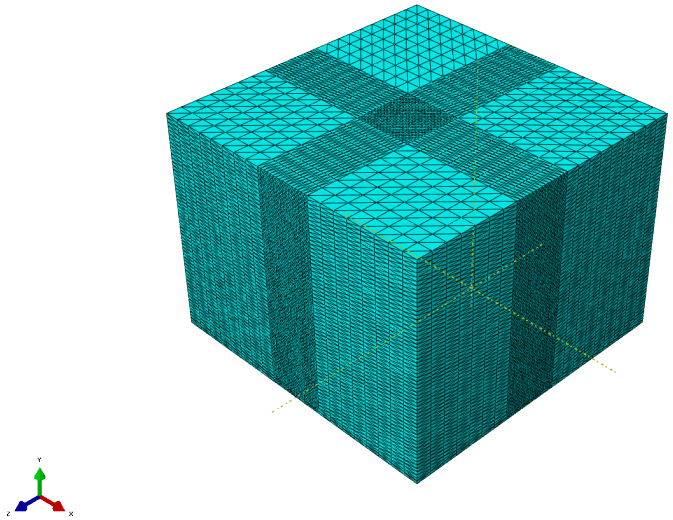

Figure 5.4.1 Mesh of the Entire Domain 3D view (θ=0°)

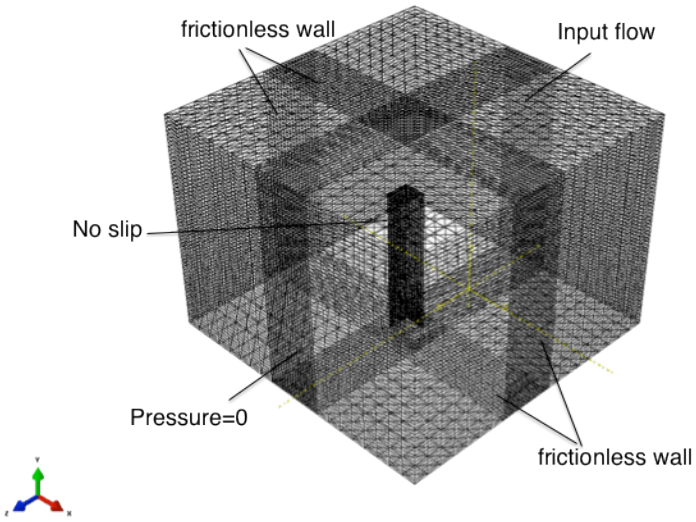

Figure 5.4.2 Mesh of the Entire Domain Transparent View (θ=0°)

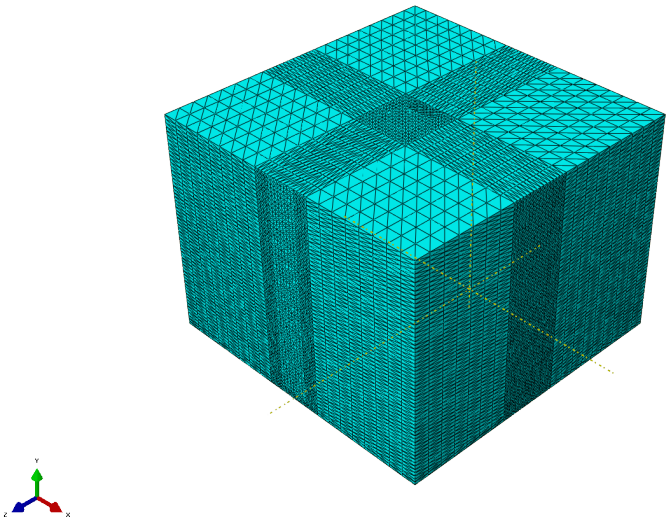

Figure 5.4.3 Mesh of the Entire Domain Transparent View (θ=45°)

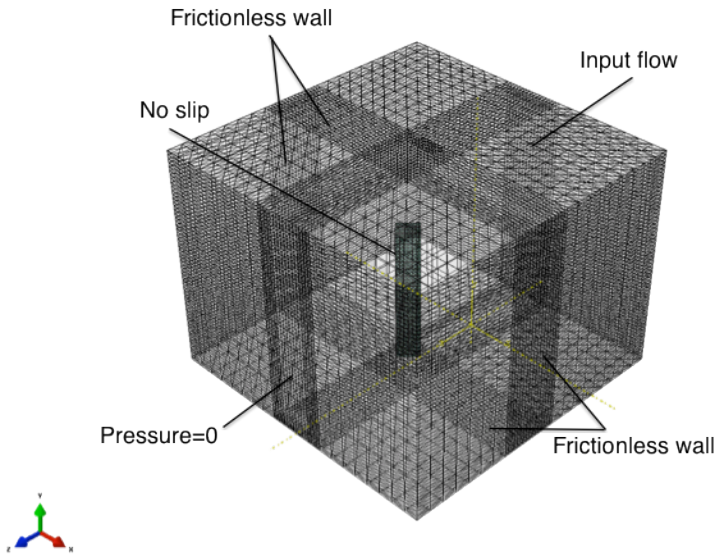

Figure 5.4.4 Mesh of the Entire Domain Transparent View (θ=45°)

In this study, the methodology for investigating the coupled fluid-structure interaction of wind flow through a cantilever building was demonstrated. The staggered FSI solution approach was implemented using Abaqus/Standard as the structural solver and Abaqus/CFD as the incompressible Navier-Stokes solver. The case study demonstrates the efficacy of multiphysics capabilities within Abaqus in studying structural, fluid and strongly coupled dynamics of wind flow and isotropic simulated building with nearly identical fluid-solid density ratios. The stability of the strongly coupled FSI problem is ensured with a fixed step algorithm within a staggered solution paradigm without resorting to iterative strategies.

Boundary conditions are defined as what is shown in Figure 5.4.2 for θ=0° and Figure 5.4.4 for θ=45°. To clarify, input flow detailed in previous section is at z-axis direction.

Zero pressure on the boundary on the other side of the model, face to input flow boundary. Surface of the structure is assumed smooth and in no slip condition, which allows no penetration or friction velocity on the surface. Other sides are frictionless wall condition with enough distance from the structure to allow turbulence vortices develop without influence from the boundary by checking on all fluid fields and results to get convergence state.

Figure 5.4.5 shows the velocity isolated face view from steady state. In the result of large amount output variable, most results from the CFD analyses are shown with figures in Appendix A.

From Figure 5.4.5 to Figure 5.4.10 are all with basic wind velocity of 51m/s. Solutions of other velocities would be discussed in the next section.

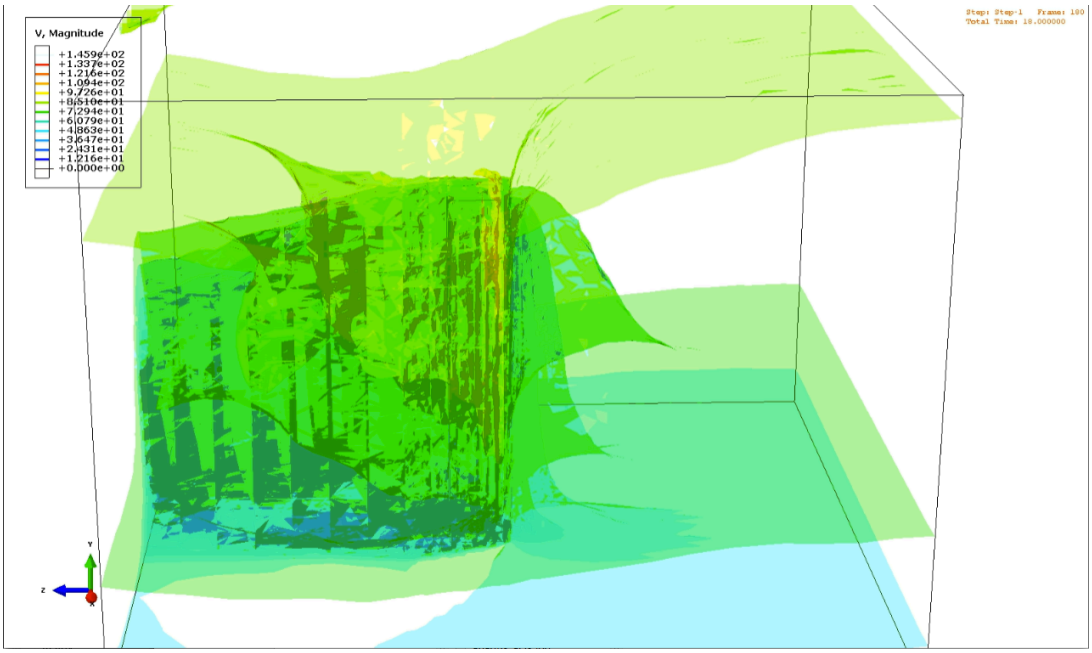

Figure 5.4.5 Velocity Magnitude Isolate Face View

From the velocity magnitude results, one can easily find increasing wind speed region around the surface of the structure without the influence of boundaries of the entire domain. Figure5.5.3 is only a magnitude distribution in which more complicated wind flow actions like vortex may not be observed.

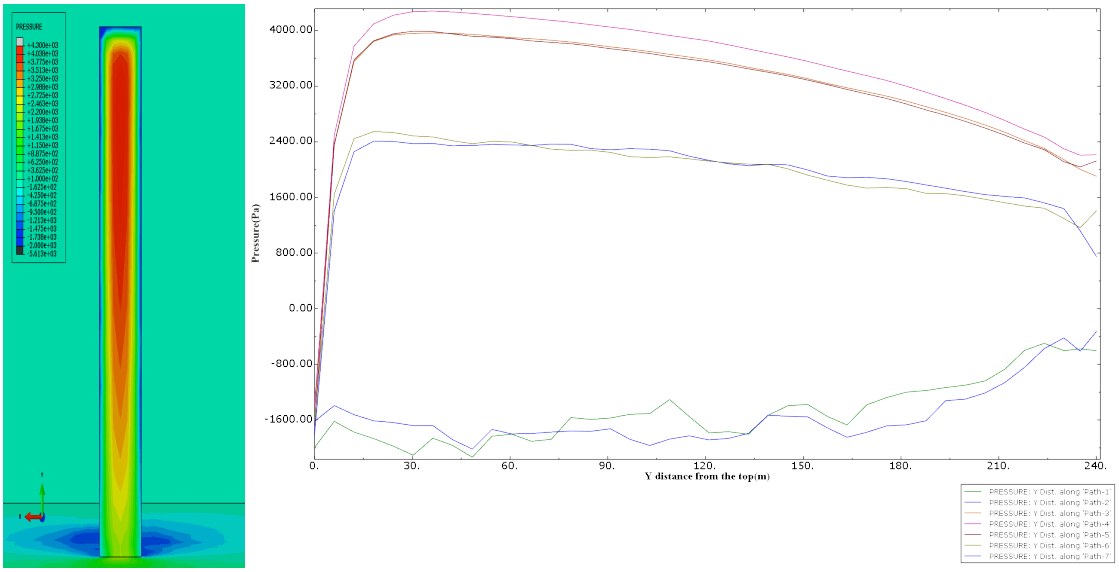

Figure 5.4.6 Pressure Magnitude in Windward Face of the Structure

Engineers are more likely consider the influence from the wind rather than the wind flow itself. Figure 5.4.6 is a fluid pressure distribution alone height of the windward face. The highest magnitude of the pressure is from the center of the facade while negative ones from edge of both sides of the front face.

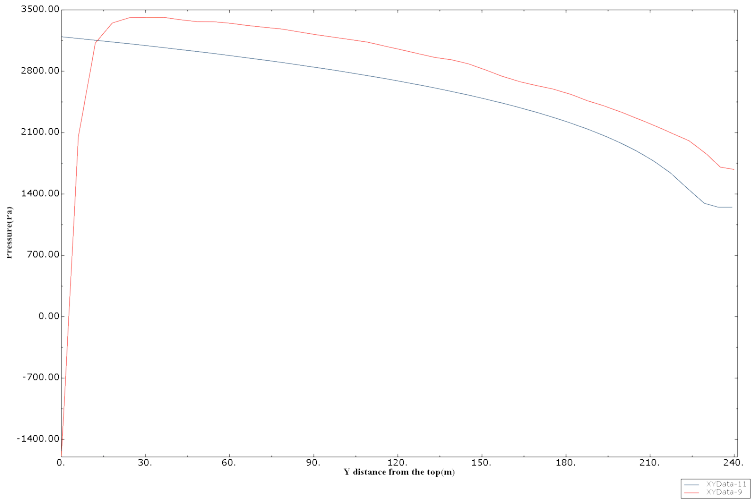

Figure 5.4.7 Pressure Average in Figure 5.5.4 Compare with ASCE 7 Wind Pressure

Pressure distribution alone the height from CFD modeling is the red curve which distinct with ASCE 7 code wind pressure near the top area of the building significantly, in which case is predictable as negative pressure from accelerated wind speed at the top edge. Magnificence of this phenomenon is highly influenced by mesh grids, time steps and turbulence model picked in the analysis. However, for a blunt body structure in this work the result is considered as a valid one.

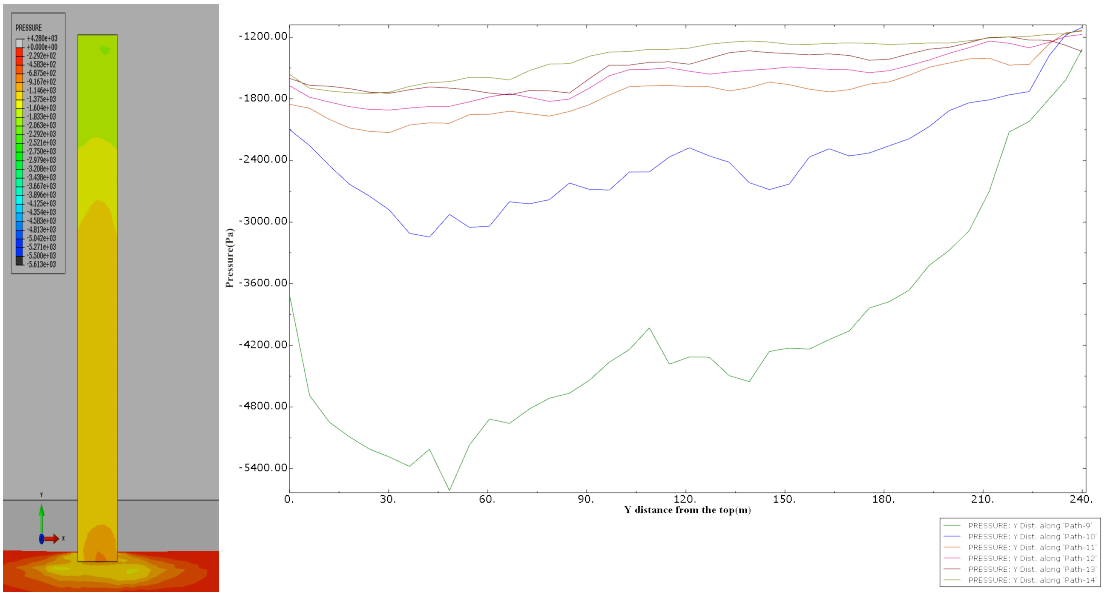

Figure 5.4.8 Pressure Magnitudes in Leeward Face of the Structure

The negative pressure with higher absolute value is a center of the face while the pressure ascending from center to edge in Figure 5.4.8, which is the leeward wall of the structure. This is a difference can be hardly ignored by an averaged negative pressure in most wind code, since higher bending momentum indication. Top and sidewall pressure (nearly symmetry for both sidewalls of the structure) are also plotted in Figure 5.4.9 and Figure 5.4.10. An important point has to be made is the influence from the wind flow distinction is highly determinate from the geometry and surrounding structures. In real cases, 240m structures standing alone at a perfectly horizontal paralleled domain as described may not be observed; this is the main reason of simulating wind flow numerically, to be able to solve for infinite practical cases.

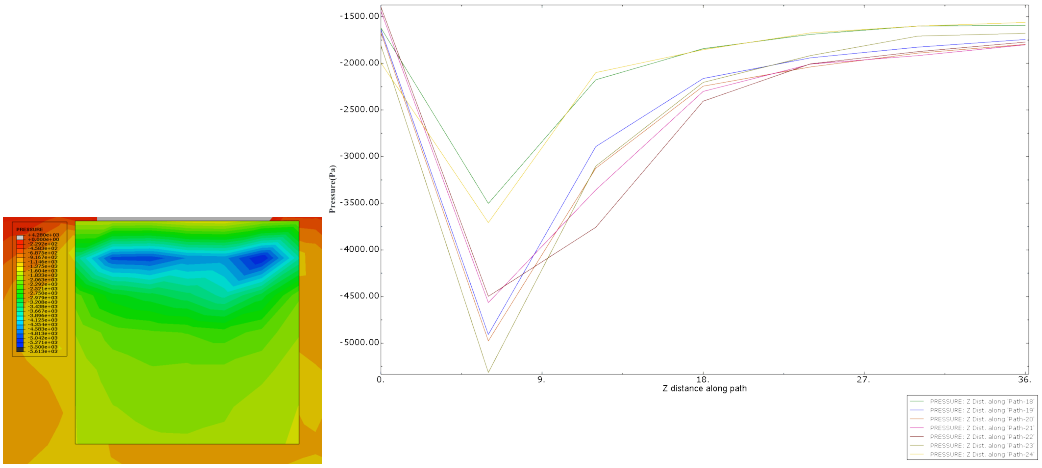

Figure 5.4.9 Pressure Magnitude in Top Face of the Structure

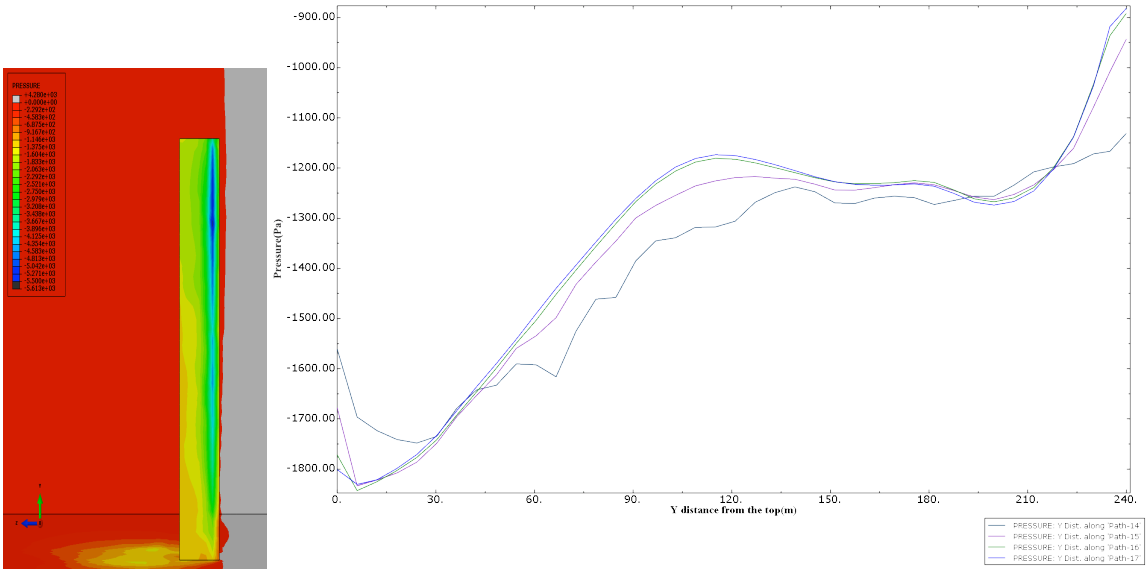

Figure 5.4.10 Pressure Magnitude in Sidewall Face of the Structure

With all assumptions and simulations made above, eventually output set in Eqn. (5.1.11). Figure 5.6.1 shows a pressure load distribution significantly differs from which can be observed from Figure 2.5.2. The numerical analysis gives a more detailed and a vibrational contour other than horizontally uniform and vertically increasing pressure distribution, so is Figure 5.6.2 top pressure, Figure 5.6.3 leeward wall pressure and Figure

5.6.4 sidewall pressure.

Compare Figure A3 with Figure 3.5.6, one can easily find, in CFD simulation, both transverse and perpendicular direction motion. Dynamic behavior can be hardly compared with static behavior of a structure. One can recognize background and resonant parts of the building displacement motion. In sacrifice of exact natural frequency of structures in different damping ratios, one can still see the background part is a neighborhood of quasi-static pressure obtained in section 3.5.

Meanwhile, in Figure B1, Figure B2, maximum velocity and acceleration in steady state is around 0.4m/s and $2m/s^2$ with structural damping less than 1%. Higher damping will enhance structural resistance to these terms.

5.5 Dragging Coefficient

With five different basic wind velocities pick from ASCE 7-10, varying top displacements can be graphed in Figure 5.6.5. In this work, attack angle of zero and forty-five degree are used in analysis, since only net force introduced maximum displacements are tracked in comparisons.

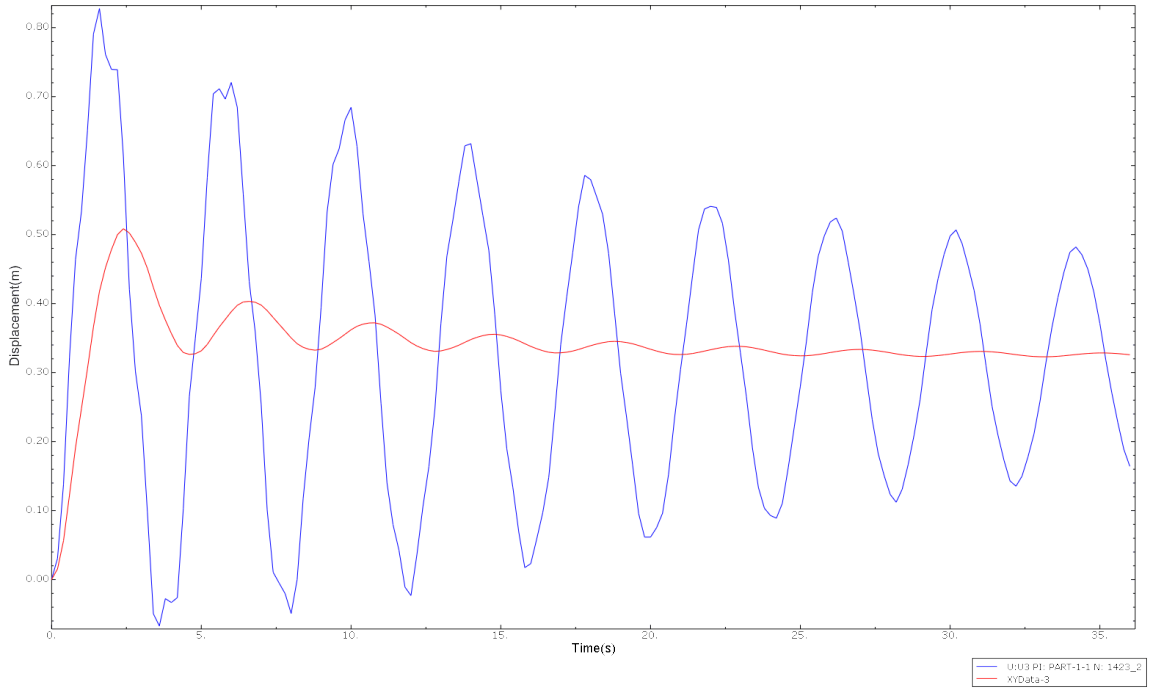

Figure 5.5.1Top Displacement (Blue) and Current Average Top Displacement (Red) vs. Time

The main reason why displacements are utilized so often is that displacements are more easily get into convergence and be considered mostly in serviceability design. Simply apply beam theory on input wind profile developed in chapter 2.

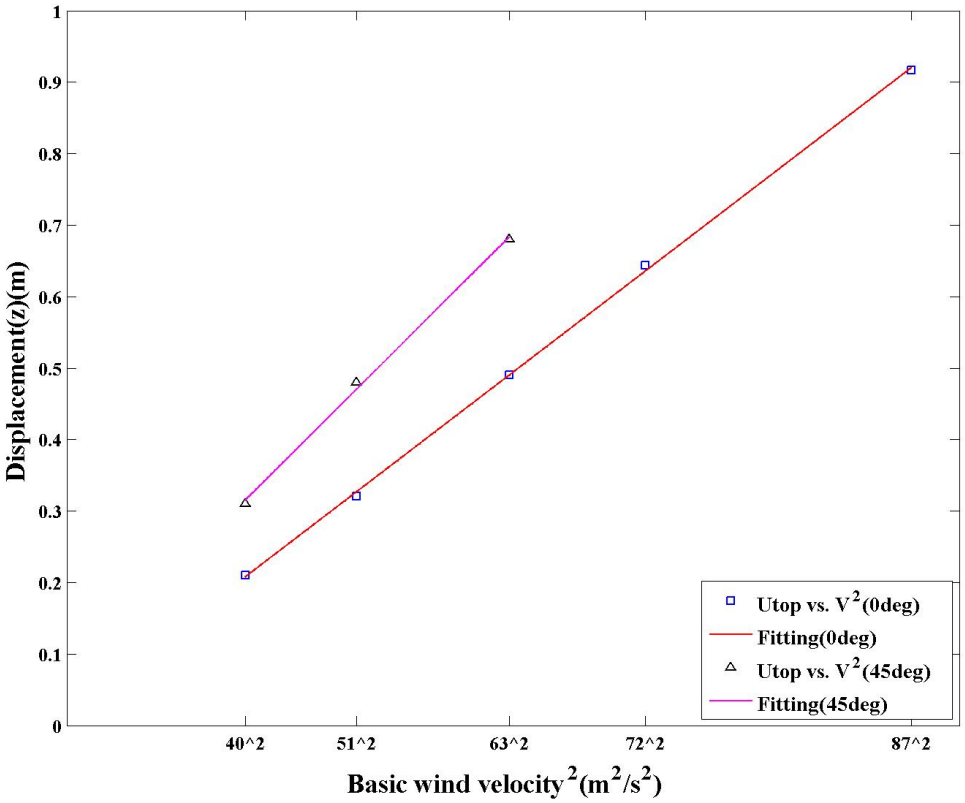

Figure 5.5.2 Top Displacement vs. Basic Wind Velocity^2

To clarify, pressure at height z is

$$p(z) = \frac{1}{2} C_d \rho V^2(z) \tag{5.6.1}$$

ρ air density;

C_d dragging coefficient;

V(z) wind velocity at height z;

Integral pressure with height to calculate shear

$$Q(z)' = p(z)B \tag{5.6.2}$$

B width of the face vertical to wind velocity, for θ=0°, B=36m, for θ=45°, $B = 36\sqrt{2}$ m;

Obtain momentum varying with height

$$M(z)' = Q(z) \tag{5.6.3}$$

And the rotation with Timoshenko beam model is

$$w'(z) = \theta(z) = \frac{M(z)}{EI} - \frac{Q(z)}{GA} \tag{5.6.4}$$

E is young's modulus;

I is moment of inertia, same constant for θ=0° and θ=45°;

G is shear modulus for poison's ratio of 0.3;

A cross sectional area;

Deflection is

$$w(z) = \int_z^H \theta(z)\, dz \tag{5.6.5}$$

Detailed calculations are calibrated with Matlab code. w(H) is the top displacement computed with the equivalent wind force in proportional to the square of the wind velocity alone with height. This ratio between wind force and velocity is defined a dimensionless number, dragging coefficient C_d, which is widely applied in wind engineering. Even though, dragging coefficient is not a constant mostly for different Reynolds numbers. And computation of Reynolds number for a complicated system itself would come with all kinds of assumptions and approximations, which might be misleading and inaccurate. However, for most airflow in engineering especially with high

velocities to introduce magnificent response of the structure, significant turbulent vortices would under certain condition relate structure and wind velocities linearly.

Table 5.5.1 Dragging Coefficients

Angle of attack (°)	Dragging coefficient C_d
0	0.9
45	0.9

With logarithm wind profile and dragging coefficients, wind load can be easily approximated with some simple calculations. However, dragging coefficients cannot be tested and hard to compute from equivalent force, which is deducted with beam theory from responds of the structure. As a matter of fact, the dragging coefficients might be practical at early stage of the analysis or a dimension less factor for comparison.

6 SUMMARY AND RECOMMENDATIONS

6.1 Summary of the Current Work

In order to study wind load on high-rise buildings, a simply case of the wind load applied on a high-rise square-plane building is analyzed. The diagrid building is designed in serviceability with stiffness-based methodology and assumed be built in Arizona. After designing the structure, different wind loads varying from 40m/s to 87m/s is applied on this structure to study the relationship between wind loads and structure responds.

With the CFD module in Abaqus, the 3D wind load analysis provide wind loads considerably more complicated than wind code of ASCE 7-10. However, with the computational power of accessible computer, assumptions on both fluid and structure made. Testing domain is finite in volume. The numerical analysis results are independent from mesh size, time step length and distance from structure to boundaries. Horizontally homogenous boundary layer produces a constant ground aerodynamic roughness. The input flow is modified with HHTBL, as the reason why ground in the model is made frictionless. Linear isotropic hollow slender beam is used instead of detailed structure. No slip condition at surface of the build without influence of openings and claddings. RNG k-ε turbulence model Abaqus is applied. Small damping of the structure is assumed. Time average displacements are used in comparison to wind codes.

Even though dragging coefficient of this specific case has been calculated with Timoshenko beam, it is not necessary in doing CFD analysis. Dynamic responds of the

structure are not considered in avoid of numerical error in the first few time steps when fluid transforming into steady state. Time average values of displacements on top of the building are used in comparison with current codes, since serviceability design considered mostly top displacements on high-rise building and wind profiles are more commonly in the form of statistic data other than time dependent ones.

All in all, this work focused on numerical analysis of wind load on a high-rise square plan building in comparison with wind code. In the author's opinion, CFD modeling in wind load on blunt body like structure is considered a valid prediction and an effective methodology.

6.2 Recommendations for Future Work

It is obvious that there are always supplements on assumptions and methodologies to enhance model behavior in numerical analysis. The k-ε turbulent model overestimates the turbulent kinetic energy at high amount region in comparison with ASCE 7-10. With higher order or non-linear ones would enhance that part. Especially, the simply most HHTBL wind flow is what applied in this wind load analysis. Wind in real word is highly comprehensive and could not be totally predicted no matter how fast a computer we use. With restrain of computational capacity and program limitation, current study has pushed the computational model near the up limit of accessible tools. The advantage of numerical method is all details of subject could be modeled in one way or another with a relatively lower price and shorter time period than widely used experiments like wind tunnel testing. With the rapid development of computational tools nowadays, wind load analyses with CFD will get higher performance and lower inaccuracy for certain in the near future.

On the other hand, developments of structure, for example, more complicated geometry, interactions of multiply subjects and increasing height are all challenges to the wind-engineering field. The wind load increment due to height of the structure has been known since prehistory. The wind load is one of the dominant factors limits the height of tall structures engineers can build. The analytical and experimental methods on wind load analysis will remain critical to decisions of engineers. However, CFD are considerably a

feasible way to make assumptions at early stage of complicated analysis; and it is also a useful tool for understanding and simulation. Based on of large amount of cases and studies, it is possible for CFD behave as reliable as solid stress analysis nowadays.

REFERENCES

[1]. Ali, M. M. & Moon, K. (2007). Structural Developments in Tall Buildings: Current Trends and Future Prospects. Architectural Science Review, Vol. 50.3, pp. 205-223.

[2]. Moon, K., Connor, J. J. & Fernandez, J. E. (2007). Diagrid Structural Systems for Tall Buildings: Characteristics and Methodology for Preliminary Design, The Structural Design of Tall and Special Buildings, Vol. 16.2, pp. 205-230.

[3]. Keith D. Hjelmstad. Fundamentals of structural mechanics. Springer 2005.

[4]. Clough, R.W. and Penzien J. Dynamics of Structures, McGraw Hill Kogakusha, 1975.

[5]. Bentley. Technical Reference Manual.Staad.pro v8i.

[6]. Bentley. STAAD.Pro Advanced Training.Staad.pro v8i.

[7]. Connor J. 2003. Introduction to Structural Motion Control. Prentice-Hall: Englewood Cliffs, NJ.

[8]. Indrajit Chowdhury and Shambhu P. Dasgupta. Computation of Rayleigh Damping Coefficients for Large Systems. The Electronic Journal of Geotechnical Engineering, Vol. 8 (2003)

[9]. Brutsaert W. (1991). Evaporation in the Atmosphere. Dordrecht, Kluwer Academic Publishers

[10]. Mark z. Jacobson. Fundamentals of Atmospheric Modeling Second Edition.© Cambridge University Press 2005

[11]. Monin A. S. and Obukhov A. M. (1954). Basic laws of turbulent mixing in the ground layer of the atmosphere. Trans. Geophys. Inst. Akad. Nauk USSR 151, 1963–87.

[12]. American Society of Civil Engineers, ASCE 7-10, Minimum Design Loads for Buildings and Other Structures, Reston, VA, 2010.

[13]. Philip Line, William L. Coulbourne,, ASCE 7-10 Wind Provisions and Effects on Wood Design and Constructio, Line/Coulbourne

[14]. A.G. Davenport and M.A.Sc. The application of statistical concepts to the wind loading of structures. Discussion on statistical concepts in wind loading of structures(1961).

[15]. Businger J. A., Wyngaard J. C., Izumi Y., and Bradley E. F. (1971) Flux-profile relationships in the atmospheric surface layer. J. Atmos. Sci. 28, 181–9.

[16]. Hinze J. O. (1975) Turbulence: An Introduction to its Mechanism and Theory, 2nd edn. New York, McGraw-Hill, 790pp.

[17]. Stull R. B. (1988) An Introduction to Boundary Layer Meteorology. Dordrecht, Kluwer Academic Publishers.

[18]. Deardorff J. W. (1972) Numerical investigation of neutral and unstable planetary boundary layers. J. Atmos. Sci. 29, 91–115.

[19]. EN 1991-1-4: Eurocode 1: Actions on structures - Part 1-4: General actions - Wind actions

[20]. Kolmogorov, A. N. (1941). de l'Academic des Sci. de 1'URSS 30:301.

[21]. C.A.J Fletcher. Computational Techniques for Fluid Dynamics, volume I. Springer-Verlag, Heidelberg, second edition, 1991

[22]. C.A.J Fletcher. Computational Techniques for Fluid Dynamics, volume II. Springer-Verlag, Heidelberg, second edition, 1991

[23]. J.H.Ferziger et al. Computational Methods for Fluid Dynamics. Springer-Verlag, Heidelberg, second edition, 1999

[24]. Abaqus Analysis v6.12 Documentation, Simulia

[25]. Masami Sato, and Takaya Kobayashi. A fundamental study of the flow past a circular cylinder using Abaqus/CFD

[26]. J. Donea et al. Arbitrary Lagrangian–Eulerian Methods. Encyclopedia of Computational Mechanics Volume 1: Fundamentals. 2004

[27]. Gene Hou1, Jin Wang2, and Anita Layton3.Numerical Methods for Fluid-Structure Interaction-A. Commun. Comput. Phys. Vol. 12, No. 2, pp. 337-377 2012.8

[28]. Young, A. D. (1989). 'Boundary layers.', BSP Professional Books, Blackwell Scientific Publications Ltd., Oxford, UK.

[29]. Stephen B. Pope. (2000). 'Turbulent flows', Cambridge University Press

[30]. Chakrabarti, S. K. (Ed.), Numerical Models in Fluid Structure Interaction, Advances in Fluid Mechanics, Vol. 42, WIT Press, 2005.

[31]. Dowell, E. H. and Hall, K. C., Modeling of fluid-structure interaction, Annual Review of Fluid Mechanics, Vol. 33, 2001, pp. 445-490.

[32]. Morand,H.J.-P.andOhayon,R.,Fluid-StructureInteraction:AppliedNumericalMethods ,Wiley, 1995.

[33]. Tennekes, H. and Lumley, J. L. (1972). 'A first course in turbulence.', The MIT Press, Cambridge, UK.

[34]. C.H.K. Williamson and R.Govardhan. (2004) 'Vortex induced vibrations'. Annu. Rev. Fluid Mech. 2004. 36:413–55

[35]. Bert Blocken, Ted Stathopoulos, Jan Carmeliet. CFD simulation of the atmospheric boundary layer: wall function problems. Atmospheric Environment 41 (2007) 238–252

[36]. Peskin, C. S., Numerical analysis of blood flow in the heart, Journal of Computational Physics, Vol. 25, 1977, pp. 220-252.

[37]. Peskin, C. S., The immersed boundary method, Acta Numerica, Vol. 11, 2002, pp. 479-517.

[38]. Haug, E. J., Intermediate Dynamics, Prentice Hall, 1992.

[39]. Malvern L W. Introduction to the Mechanics of a Continuous Medium. Prentice-Hall: Englewood Cliffs, 1969.

APPENDIX A

DATA COLLECTED MARCH-MAY 2014

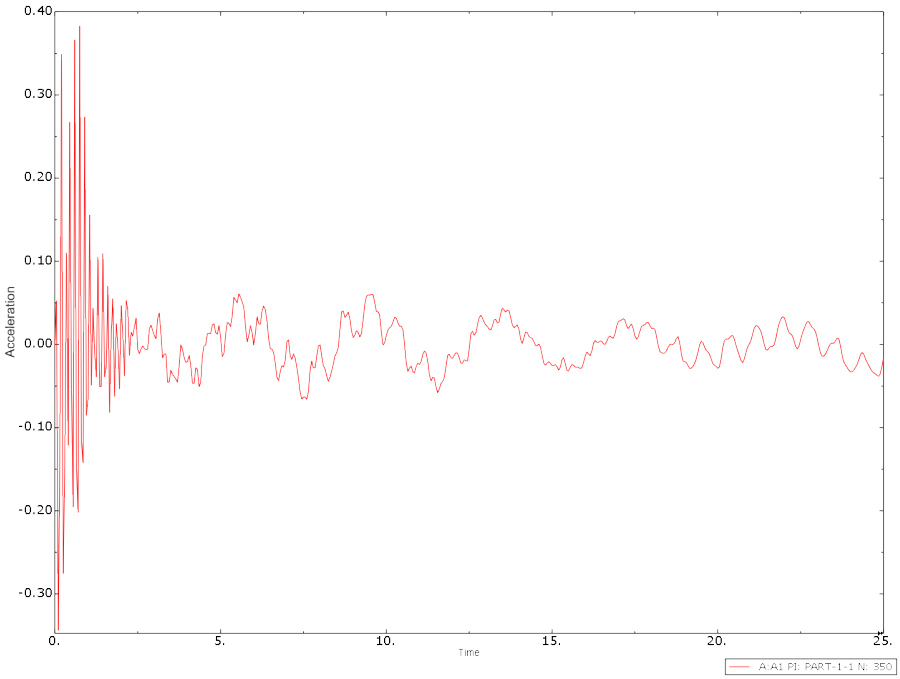

Figure A1 (a) Acceleration(x) of Top Center Node

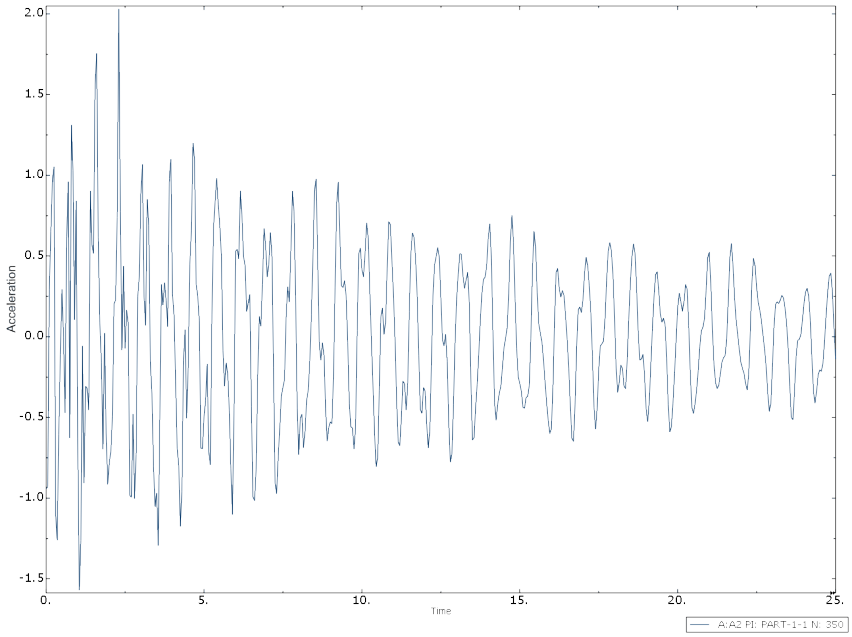

Figure A1 (b) Acceleration (y) of Top Center Node

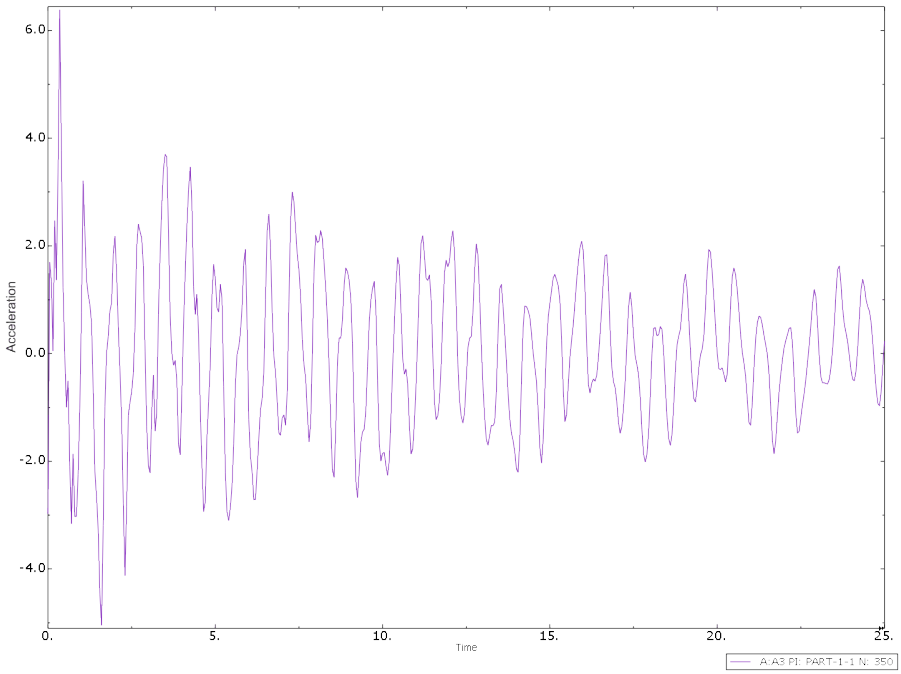

Figure A1 (c) Acceleration (z) of Top Center Node

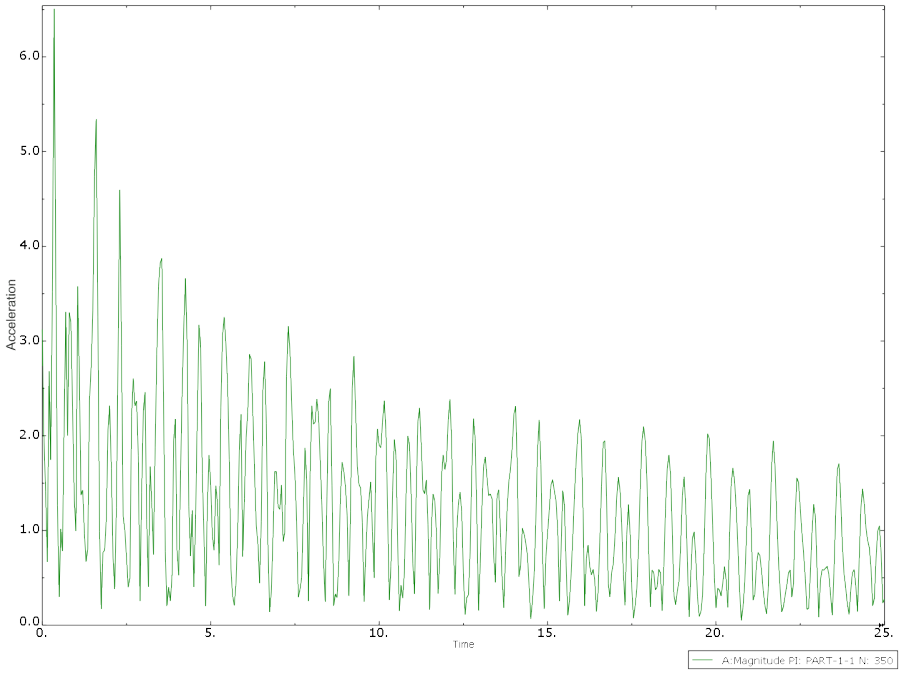

Figure A1 (d) Acceleration (Magnitude) of Top Center Node

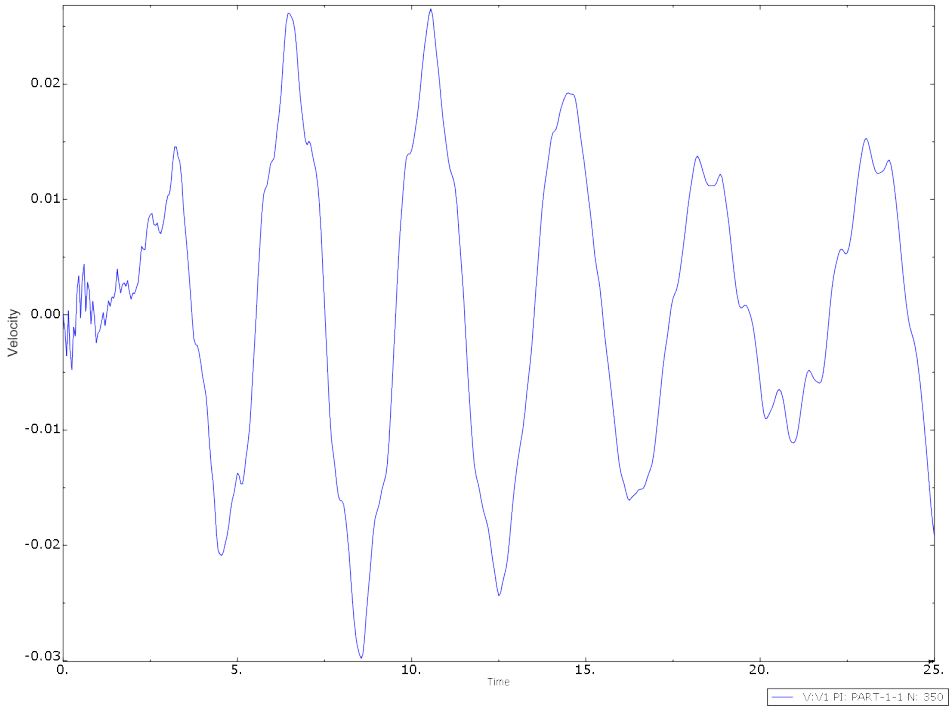

Figure A2 (a) V (x) of Top Center Node

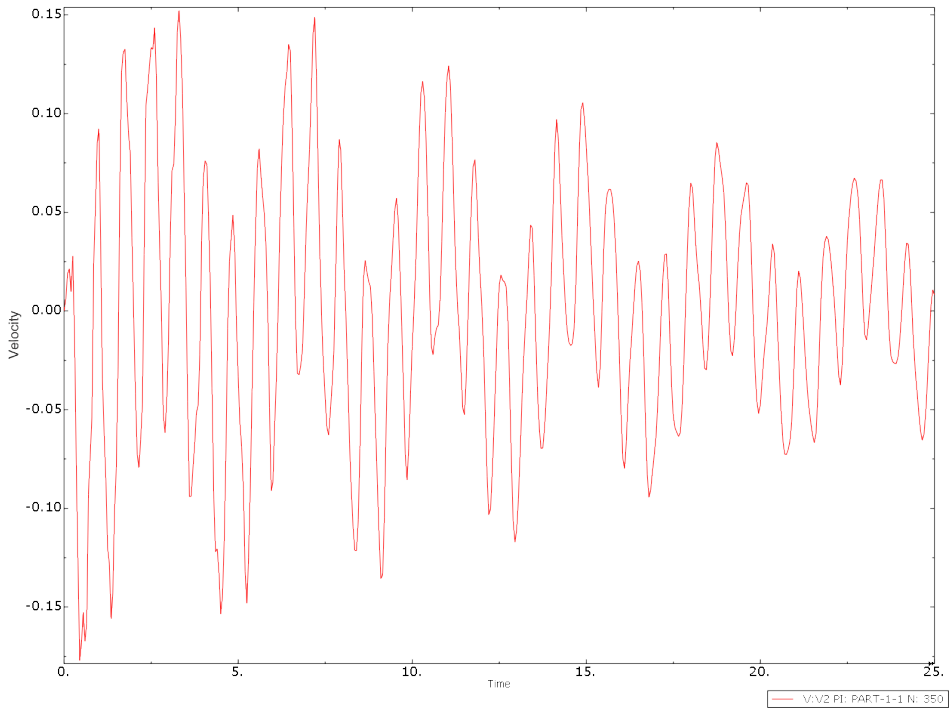

Figure A2 (b) V (y) of Top Center Node

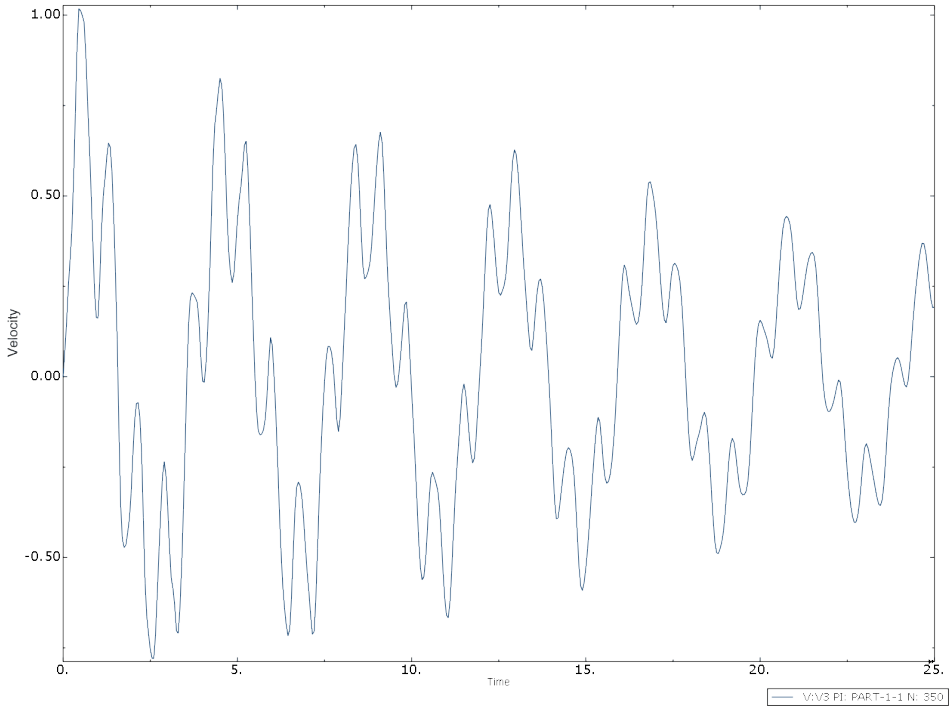

Figure A2 (c) V (z) of Top Center Node

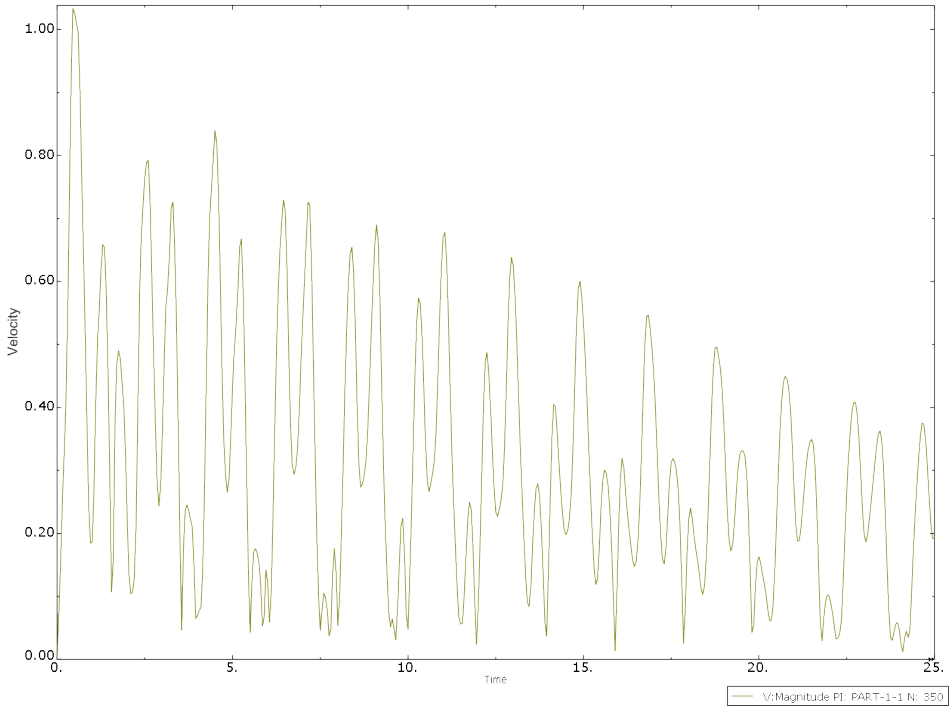

Figure A2 (d) V Magnitude of Top Center Node

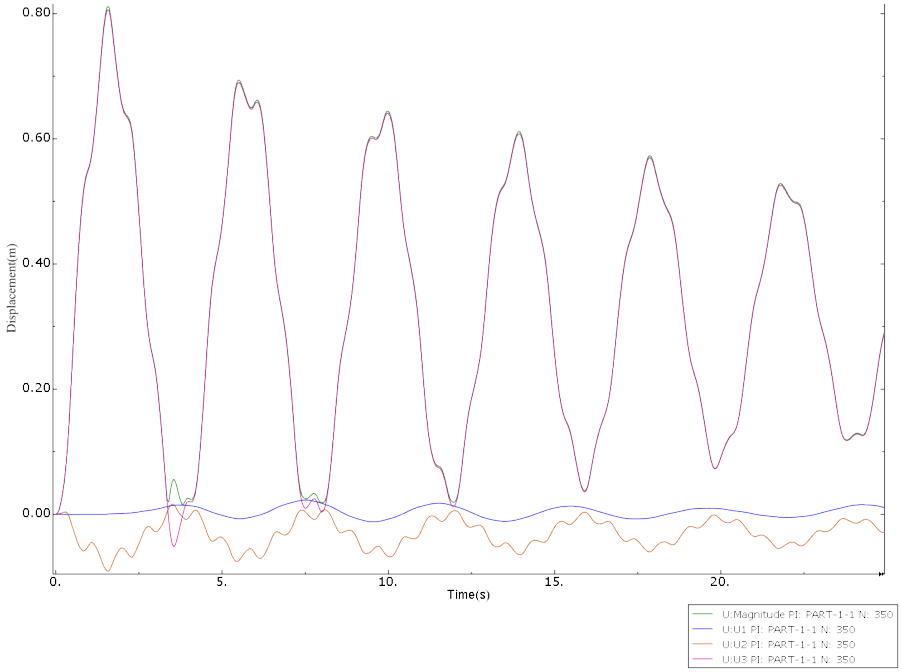

Figure A3 Displacements of Top Center Node

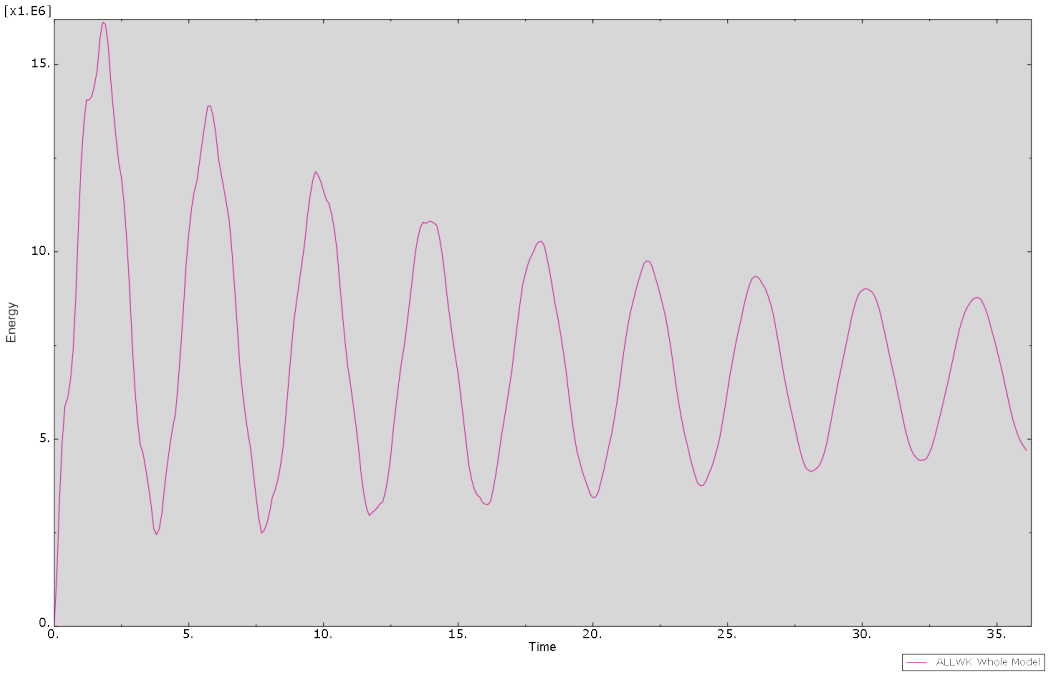

Figure A4 External Work of the Structure

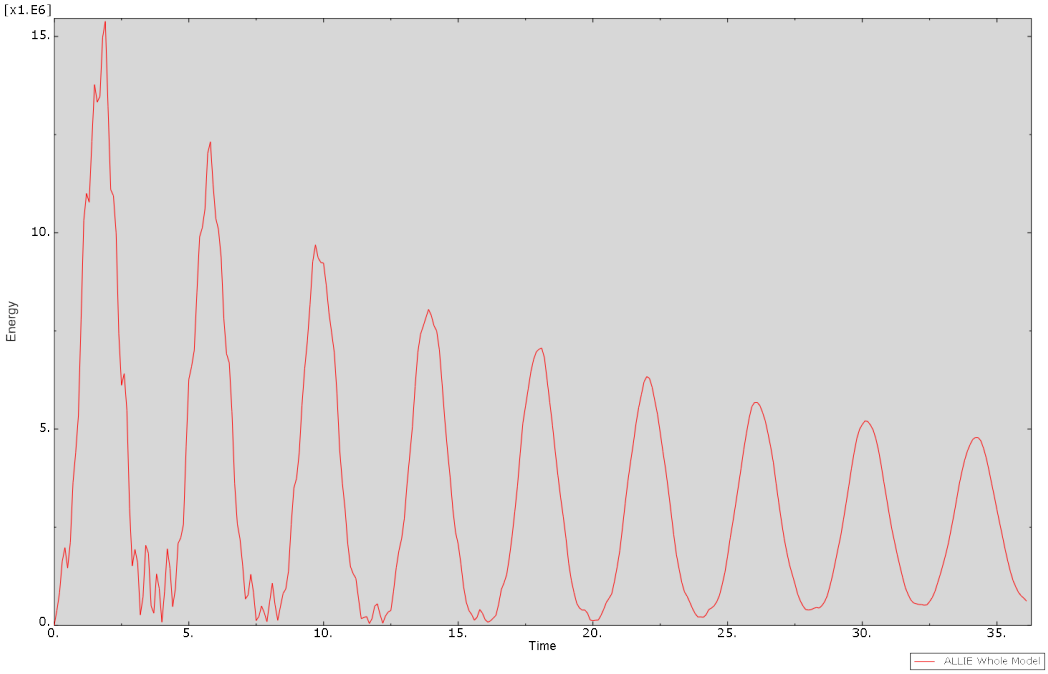

Figure A5 Internal Work of the Structure

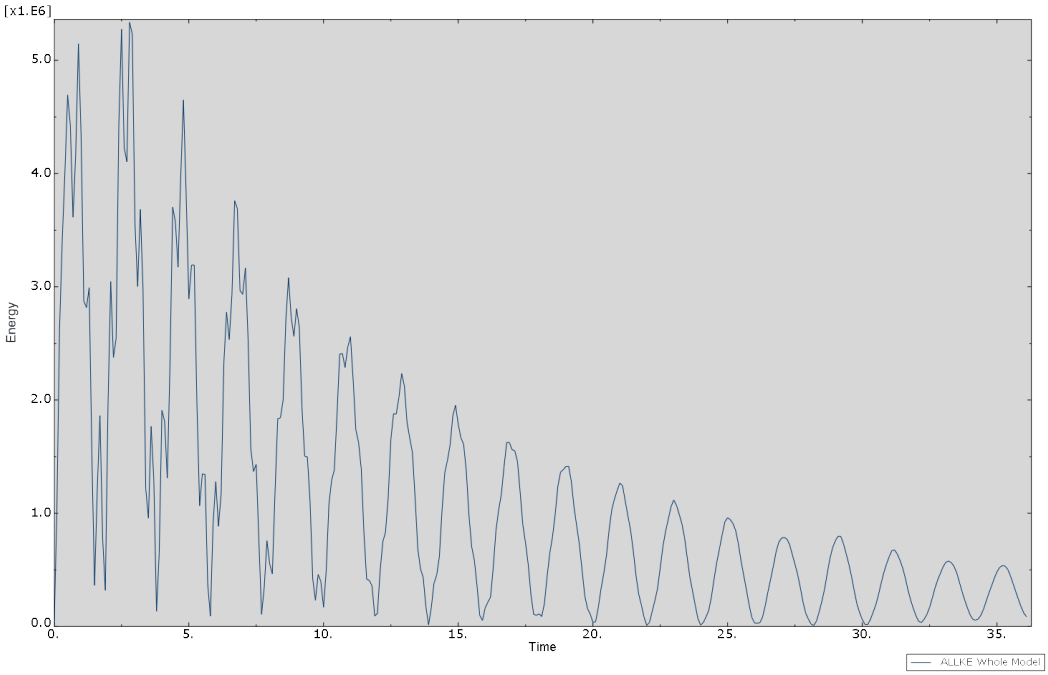

Figure A6 Kinetic Energy of the Structure

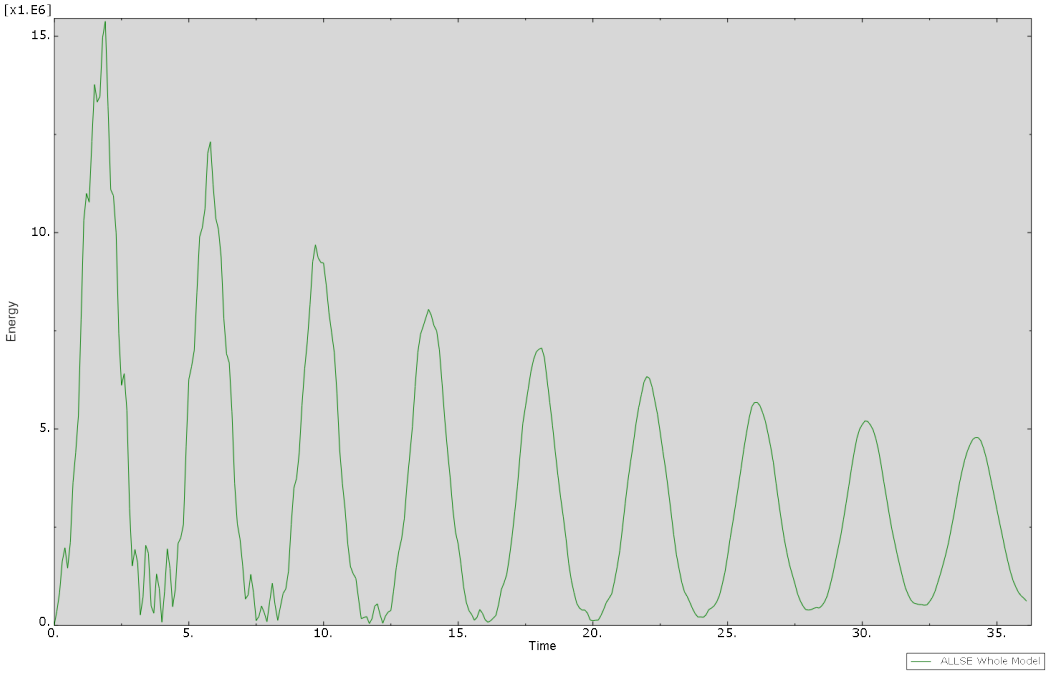

Figure A7 Strain Energy of the Structure

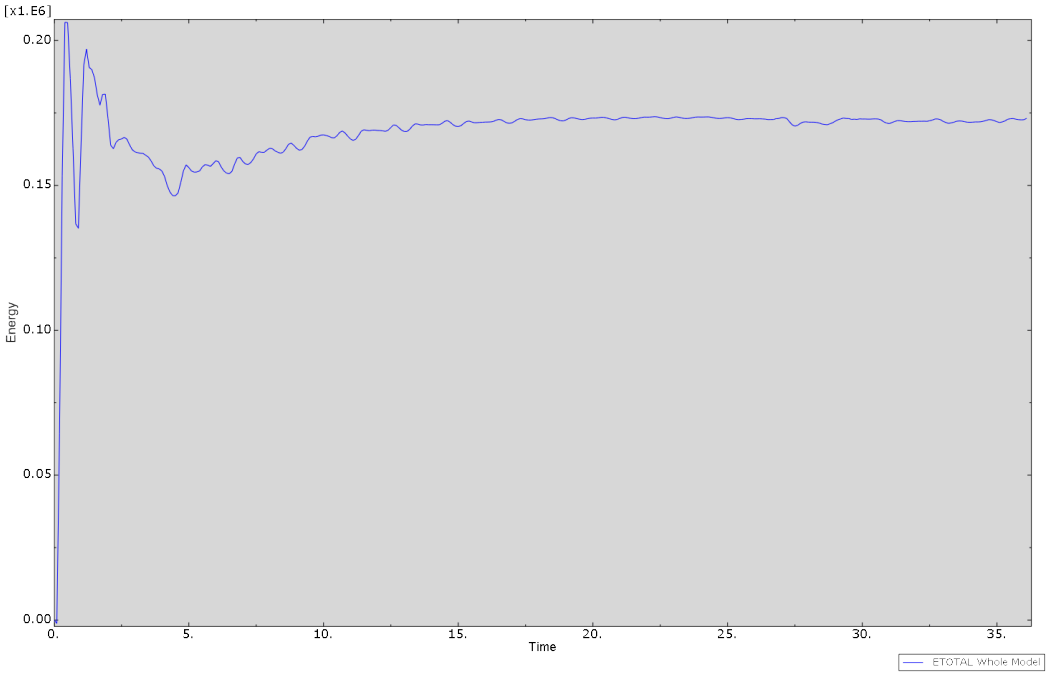

Figure A8 Total Output Set Energy of the Structure

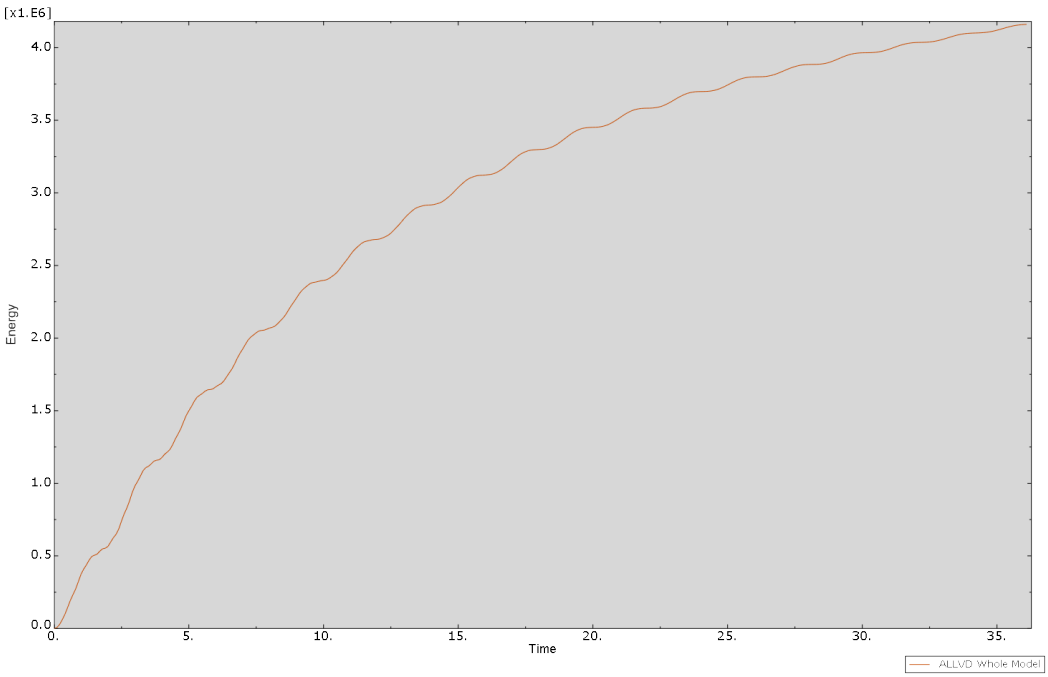

Figure A9 Viscous Dissipation Energy of the Structure